UNIVERSITY OF CALIFORNIA, SAN DIEGO

An Investigation into the Postbuckling Response of a Single Blade-Stiffened Composite Panel

A Thesis submitted in partial satisfaction of the requirements

for the degree of Master of Science

in

Structural Engineering

by

Alexander Daniel Spediacci

Committee in Charge:

Chiara Bisagni, Chair
Hyonny Kim
Yael D. Van Den Einde

2014

The Thesis of Alexander Daniel Spediacci is approved and it is acceptable in quality and form for publication on microfilm and electronically:

_____

_____

_____

Chair

University of California, San Diego

2014

Table of Contents

List of Figures

List of Tables

Acknowledgements

I would like to thank Professor Chiara Bisagni for her guidance, and serving as chair of my thesis committee. Her patience and insight throughout the thesis writing process has been invaluable.

I would also like to thank Dr. Kim and Dr. Van Den Einde for their support, and serving on my thesis committee.

In addition, I would like to thank my family, friends, and colleagues for their support and suggestions throughout the thesis writing process.

ABSTRACT OF THE THESIS

An Investigation into the Postbuckling Response of a
Single Blade-Stiffened Composite Panel

by

Alexander Daniel Spediacci

Master of Science in Structural Engineering

University of California, San Diego, 2014

Professor Chiara Bisagni, Chair

The large strength reserves of stiffened composite structures in the postbuckling range appeal to the aerospace industry because of the high strength-to weight-ratio. Design and analysis of these large-scale, complex structures is technical, and requires major computational effort. Using the building-block approach, a smaller, single-stringer panel can be a useful and efficient tool for initial design, and can reveal critical behavior of a larger, multi-stringer panel.

A characterization, through finite element modeling, of buckling and postbuckling response of a single blade-stiffened composite panel is proposed. Several factors affecting buckling and postbuckling behavior are investigated, including specimen length, initial imperfections, mode switching, and skin stringer separation. Two specimens are repeatedly tested under quasi-static compression loading well into the postbuckling range, showing no sign of damage. The test data from the specimens are used to compare and validate the nonlinear finite element models, show good correlation with the models. Ultimately, this work will serve to demonstrate the safety of stiffened structures operating in the postbuckling range and allow for thinner, lighter structures, which can increase the overall efficiency of aircraft.

Chapter 1 - Introduction

1.1 - Background

Lightweight materials and engineering techniques are paramount in the aerospace industry. Over the last few decades, the use of composite materials in aircrafts has significantly increased. This has led to an increase in the complexity of the design and analysis process. The need for lighter, stiffer, and stronger structures leads to thinner, more structurally efficient components.

Composite materials, specifically fiber-reinforced polymers, have several benefits over metallics. The high strength-to-weight ratio of composites, and tailor-able directional properties make composite materials ideal for aerospace structures. The complex geometry of many aerospace components can potentially be easy to fabricate from composite materials. Since composite materials tend to have high fatigue resistance relative to metals, they can have a longer service life, which reduces overall lifetime cost.

The complexity of composite materials however, introduces many complications to their use. Unlike metallics, composites are anisotropic, exhibit complex failure modes, and are sensitive to hygrothermal loads. The anisotropic behavior requires complex analysis methods and complex methods for determining failure. One of the most susceptible forms of degradation within a composite material is delamination, or separation of plies through the thickness of the laminate. This type

of failure can greatly reduce the strength of the composite laminate, and requires complex inspection methods to detect.

Fuselage and wing structures are increasingly being designed and built out of composite materials, rather than metals. The curved, thin-walled structure of a fuselage or wing is subjected to shear, bending, and torsional loads. These thin-walled skins are highly sensitive to imperfections under these loading conditions, which causes them to buckle at very low load levels. To strengthen and stiffen the skin, periodically placed composite stringers are used. The stringers are also made of composite materials, and are either co-cured with the skin or are bonded to the skin after curing. Stringers come in many types, such as: hat stringers, I-stringers, J-stringers, or blade stringers. One main purpose of the stringers is to increase the moment of inertia of the skin, in order to hold the skin in place past the point of buckling. This phenomenon, called postbuckling, is the ability to carry loads beyond the critical buckling load.

These stiffened structures exhibit local buckling of the skin at a fairly low load level, but may remain undamaged well into the postbuckling range. The postbuckling range can be several times greater than the linear range; however, any pre-damage in the panel can significantly degrade the postbuckling capacity, leading to premature collapse. [11-14]

Predicting the buckling response and damage tolerance of stiffened structures, with and without initial damage, has been a large focus in the aerospace community.

[3, 7-15] Much of the previous research has focused on developing finite element models, and validating them with experimental tests of multi-stringer panels. However, due to the high manufacturing and testing costs, a relatively small number of panels have been experimentally tested. In addition, the computation time necessary to predict the postbuckling response, damage initiation and propagation, and collapse of the finite element models is tremendous.

1.2 - Previous Works

A proposal paper by Riks et al., [2] studies the mode switching phenomena of thin-walled shell structures. This paper describes previous experiments on compression loaded, simply supported plates and how the buckling shape propagates through the postbuckling range. The authors proposed a two-step solution method; a quasi-static response and a transition response, which cumulatively would be able to define the postbuckling response. The solutions would be able to find the location of the critical points, where the static equilibrium could no longer be maintained and the transition response would occur. The transition response incorporated the dynamic components of the mode switch, and once static equilibrium was reached, the quasi-static analysis was continued. This process was able to capture several mode switches and predict results with reasonable accuracy. However, the authors noted that the solutions given by this type of analysis may not be unique, and might depend heavily on initial conditions.

Falzon et al. [3] posed an alternative method for predicting the postbuckling mode-switching behavior of a blade-stiffened panel. A modified dynamic explicit

analysis was used instead of using a static analysis solver. This type of analysis is able to capture the mode switching of the panel and the force-displacement response. The procedure used a damping matrix with values proportional to the stiffness matrix and with velocity and acceleration varying linearly between time steps. With a quasi-static displacement applied, the method was able to accurately predict the load that corresponded to the mode switch for a multi-stringer panel test, as well as the buckled shape.

Hilburger et al. [4] studied the effect of initial imperfections on the postbuckling response of unstiffened cylindrical shells, using a method similar to Falzon et al. [3]. The study included three graphite/epoxy test cylinders with different layups. The imperfections included in the study were out-of-plane geometric imperfections, as well as thickness variations, non-uniform loading, and boundary conditions. The finite element analyses used in the study were static nonlinear analyses with a non-linear dynamic analysis implemented to follow unstable response. The test results compared well with the models and showed the response was highly dependent on the different types of imperfections within the cylinders. The study concluded that the imperfections were shown to be more significant in quasi-isotropic layups compared to orthotropic layups.

Wullschleger et al [5] performed a study on the imperfect cylindrical shells and determining the buckling load. The focus of the study was to predict the onset of buckling in a composite cylindrical shell using different finite element solution techniques. The authors determined that the exact prediction of buckling of the

cylinders required accurate measurements of nodal locations of the panels in question. Also, loading increments should be reduced near the predicted linear eigenvalue buckling load. For prediction of the onset of buckling under dynamic loading, the time step must be extremely small near the point of buckling to maintain convergence.

A study conducted by Bisagni, [6] examined the buckling and postbuckling behavior of two types of unstiffened composite cylindrical shells under axial compression. Test specimens were used to compare with the finite element results. The cylinders used had diameters of 700 mm, and layups of [0/45/-45/0], or $[45/-45]_S$. The finite element models considered the geometric imperfections of the panel, which was measured with a laser scanning system and used three types of analyses to predict the response. The different analysis methods used were a linear eigenvalue analysis to predict the buckle force and shape, a nonlinear static Riks arc-length analysis, as well as a nonlinear explicit dynamic analysis with a quasi-static loading applied. The three types of analyses had agreeable results with the test specimens, including the force-displacement response and the postbuckling behavior. The analyses carried out subsequently included varying amplitudes of imperfections to determine the sensitivity of the cylinders to larger imperfections.

The article by Zimmermann et al. [7] describes the study of eight different types of large, curved, blade-stiffened composite panels under axial compression. Three different types of panels were used in the total of eight. The differences between the types of panels were the arc radius, number of stringers, and skin thickness. The radius of the first panel was 1000 mm with 4 stringers and a skin

thickness of 0.75 mm. The second panel had a radius of 1000 mm, 3 stringers, and a skin thickness of 1 mm. The third panel had a radius of 400 mm, 3 stringers, and a skin thickness of 0.75 mm. The panels were loaded quasi-statically to collapse, with in-plane and out-of-plane displacement measured with a digital image correlation system. The force-displacement response of each type of panel was similar and validated the redundancy of this type of test. One key difference between the tests was the free edge boundary condition in the panels and how this affected the postbuckling response. Some finite element analyses were done to compare with the test results, but were only used to show the correlation possibility between the models and the experimental tests.

In 2008, Degenhardt et al. [8] conducted a similar experiment to Zimmermann et al. [7], except the panel edge conditions were more closely examined. The panel had 4 blade stiffeners with the free edges of the panels placed in potting, which maintained the straight edge throughout the postbuckling range. The panel was loaded quasi-statically to failure. A finite element analysis was done using Abaqus. The model consisted of shell elements used for the skin and stiffener and 3D elements with a stress-based failure criterion used for the adhesive layer. The degradation of the adhesive was integrated into a user-subroutine model in Abaqus. The model introduced an initial geometric imperfection of a buckling mode shape into the nonlinear analysis and was then executed to collapse. This nonlinear analysis was conducted with and without the adhesive degradation subroutine. The study concluded for multi-stringer panels subjected to loads deep in the postbuckling range

degradation of the skin-stiffener interface should be taken into account in order to determine the panels overall force-displacement response.

Orifici et al. [9] studied the effect of out-of-plane displacement on a single-stringer T-shaped cross-section. The blade stringer flanges were tapered or flat for each specimen. Finite element modeling was validated with experimental tests of bending flanges and blade sections of the cross-section. Three tests were used; one which the blade section was clamped, while the skin edges were loaded in opposing directions, which provided an overall rotation. The second test loaded both edges of the skin by pulling them away from the blade-clamp, and a third where the skin edges were pushed in the direction of the blade clamp. These types of loadings provided similar out-of-plane displacements to buckling shapes of a large multi-stringer panel, and all resulted in different failure patterns. The T-sections were also modeled in a finite element program, with the different loading conditions. Some of the failure patterns were not well predicted by the finite element analysis, but were considered to be unimportant to the failure types observed in larger multi-stringer stiffened panels.

The article “Failure Analysis in Postbuckled Composite T-Sections” by Orifici et al. [10] built upon the previous work [9]. Instead of studying tapered or flat blade stringer flanges, Orifici et al. [10] studied the strength effect of the resin overflow area at the edge of the flange, as well as initial manufacturing defects. The specimens tested were nominally identical, however had different tapers between the stringer sections, radius at the base of the stringer, and resin overflow. The finite element models were created with 3D continuum elements, with cohesive elements at the skin-

stringer interface. The study concluded that this type of model was adequate for predicting the onset and propagation of delamination between the skin and stringer; however, it was unable to predict any failure at the base of the blade. The finite element model predicted flange delamination failure to be dependent on the resin overflow at the tip of the flange; any increase in excess resin led to a decrease in overall strength. The bending failure at the base of the blade did occur in a minority of the experimental tests and led to a 15-20% decrease in strength. Although the specimens were nominally identical, they did exhibit different failure patterns.

The study conducted by Orifici et al. [11], examined the postbuckling response of two single-stringer, blade stiffened compression specimen types. The first panel type was 400 mm long, with 300 mm free length, 64 mm wide, with a blade stiffener 32 mm wide, and 14 mm tall. The second panel type had an overall length of 500 mm, 400 mm free length, 112 mm width, with a blade stiffener 56 mm wide, and 29 mm tall. Six of each panel type were tested, one with no initial damage and another with a centrally located Teflon strip, 80 mm long, and 105 mm long for each panel, respectively. The Teflon was located between the skin and stringer to simulate initial damage. The panels were tested in compression, as well as modeled in a finite element program. The finite element model consisted of a global model using shell elements to predict the overall shape and a local T-shape cross-section model, which incorporated continuum elements for the composite plies and the Virtual Crack Closure Technique (VCCT) Multi-Point Constraints (MPCs) for the interface between the skin and stringer. The continuum elements included in-ply damage propagation

capabilities. For models that included the Teflon strip, the VCCT constraints were removed at the location of the Teflon.

The experimental tests of the panels showed consistent results. The initially intact panels had a much higher load capacity than the pre-damaged panels, but instantaneously collapsed at the onset of the skin and stringer delamination. The pre-damage panels showed a progression in delaminated area, until finally the panels collapsed. Both the intact and pre-damaged panels were well characterized by the finite element models, including the panel postbuckling configurations, crack propagation in the pre-damaged panels, as well as the prediction of collapse loads.

In another study, Orifici et al. [12] used the T-section results to apply to a larger panel. The study tested two curved, blade-stiffened panels; one with no initial damage, and another with initial separation between the skin and stringers at 2 discrete locations. The panels were modeled using Marc finite element software package, with a relatively coarse mesh of approx. 6,000 shell elements. A linear perturbation analysis yielded the buckling mode shapes of the panel, which were implemented as imperfections in the nonlinear analysis. A separate analysis included the initial measured imperfections of the panel. The localized model was a representation of a cross-section of a single stringer and skin, which measured 152 mm wide by 4 mm long. This was identical to the T-sections from the previous study. The local model included intralaminar and interlaminar damage capabilities, with global-to-local boundary conditions applied as a subroutine. This allowed the local model to follow

the displacements of several discrete segments of the global panel, and provide an accurate failure initiation prediction for the global model.

The experimental test determined the failure in the intact and initially damaged panel was due to debond of the skin and stringer. Immediately following the skin stringer debond, the panel catastrophically collapsed. The finite element models yielded similar results to the experimental test; however, there was some difference in the buckled shape of the panels. Apart from the difference in shape, the finite element models successfully captured the force-displacement response and failure characteristics of the panel.

The study titled "Single-Stringer Compression Specimen for the Assessment of Damage Tolerance of Postbuckled Structures" by Bisagni et al. [13] investigated the use of a single hat-stringer model to predict the response of a larger multi-stringer panel. Based on numerical analyses of a large multi-stringer panel, a size was chosen for the single-stringer representative panel based on the buckling response similarities and damage tolerance. The single-stringer panel was taken to be 300 mm long (in the direction of the stringer), and 150 mm wide centered about the stringer. The numerical simulations were done using S4R shell elements for the skin and stiffener, approximately 0.8 mm in size with intralaminar damage propagation capabilities. Cohesive elements were used to simulate the bond between the skin and the foot of the stiffener, with interlaminar damage capabilities.

The numerical model was compared with six nominally identical panel tests. Half of the panels contained a 20 mm wide Teflon insert placed between the skin and stringer foot, to simulate an initial disbond. The numerical analyses had good correlation with the test specimens, with less than 6% error. The study concluded that the Teflon insert decreased the overall strength by 12%, and was well characterized by the model.

A study by Vescovini et al. [14] was conducted on a different numerical simplification method for the postbuckling response and damage of a hat-type multi-stringer panel. Three separate finite element models were created in Abaqus; one consisted of a global panel, and a second of a smaller, panel 300 mm long by 150 mm wide which represented the width of one stringer bay (taken as the same from Bisagni et al. [13].) A third simplified model, which consisted of half the width of the previous model, considered only the skin and stiffener foot with symmetry conditions at the center of the stringer. The single-stringer panel and the half-size model were created using shell elements and included interlaminar failure within cohesive elements between the skin and stiffener foot. The simplified model and the single-stringer model had very similar results; however, the required computation time for the simplified model drastically decreased, which allowed for mesh sensitivity studies to be completed on the simplified model, as well as the influence of different bond imperfection sizes.

Kang et al. [15] proposed an algorithm for finding the optimal weight design for a square composite panel loaded in uniaxial compression. The algorithm included

variables of: number of plies, ply orientations, and variable I-shape stiffener flange and web sizes. The panel had two I-stiffeners, located at variable locations from the edge of the panel. The most weight efficient panel had the I-flanges be the full width of the specimen, nearly creating a box. The study concluded the spacing of the stiffeners should be a factor of weight in the panel, since smaller spacing on panels with several stiffeners leads to increased weight.

1.3 - Thesis Proposal

The focus of this thesis work was to characterize the postbuckling response of a single-blade stiffened composite panel under axial compression. Abaqus finite element software [16] was used to create a model of the compression specimen. Post-processing of the test data and finite element results was done using Matlab [17]. Several parameters were examined in the finite element models, including the linear eigenvalue buckling mode shapes, nonlinear response with imperfections of mode shapes applied, examination of first-ply failure, effect of specimen length, dynamic mode switching, and the effect of the Teflon separation.

Two nominally identical panels were tested in displacement control using an MTS load frame. The MTS testing program template and setup of the test equipment was configured to test the panels with repeatability and consistency. Axial displacement and force data was recorded, as well as measurements of out-of-plane displacements. The test data was compared with the finite element modeling and propositions were made for which model parameters to include, to lead to good model correlation.

Showing the capability of the panels remaining elastic deep into the postbuckling range can serve to increase the design allowance of stiffened structures. Allowing these types of structures to operate well into the postbuckling range can lead to thinner designs, which can ultimately decrease overall weight.

Chapter 2 - Panel Description

2.1 - Nominal Panel Description

The specimens used in this test are blade-stiffened, representative of a composite wing panel. The specimen was designed according to the recommendations from Bisagni et al. [13]. Typical fuselage skins are 8-ply quasi-isotropic composite, 1 mm thick, with periodic stringers running the length of the fuselage. The pitch, or center-to-center distance between the stringers, is approximately 150 mm. The unconstrained length of the specimen corresponded with one of the local skin buckling mode shapes, taken to be 240 mm.

The nominal design specifications of the stiffened panel used in this experiment are as follows. The panel overall length was designed to be 300 mm, width of 150 mm, and a skin thickness of 1 mm. The layup of the skin was specified as 8-ply, quasi-isotropic, $[0/45/-45/90]_S$ Hexcel IM7/8552 graphite/epoxy prepreg tape, with properties shown in Table 2.1.1. The 0-degree ply was aligned with the axial direction of the panel. Each ply was specified to be 0.125 mm thick. The blade stiffener is a T-shape, centered about the width of the specimen, running in the longitudinal direction of the panel. The stiffener was composed of two symmetric L-shapes back-to-back, each L-shape contained the same layup as the skin. The stiffener section was co-cured with the panel, which did not require the use of adhesive. The blade section is perpendicular to the skin and the flanges are the sections in contact with the skin. The flanges and blade of the L-shapes are 31 mm wide. Aluminum tabs

measuring 30 mm in thickness were adhered to each end of the panel, leaving a free length of 240 mm. The panel also included a Teflon insert, 30 mm wide, placed between the skin and the stiffener to simulate a region of delamination.

Table 2.1.1: Hexcel IM7/8552 lamina properties [13]

Description	Symbol	Value
Mass Density	ρ	1.61 g/cm^3
Ply Thickness	t_{ply}	0.125 mm
Fiber Direction Modulus	E_{11}	150 GPa
Matrix Direction Modulus	E_{22}	9080 MPa
Major Poisson Ratio	ν_{12}	0.32
Shear Modulus	G_{12}	5290 MPa
Fiber Tensile Strength	X_T	2323 MPa
Fiber Compressive Strength	X_C	1200 MPa
Matrix Tensile Strength	Y_T	160.2 MPa
Matrix Compressive Strength	Y_C	199.8 MPa
Shear Strength	S	130.2 MPa

2.2 - SP-1 Panel

The measurements of the SP-1 panel are shown in Figure 2.2.1. The skin is 300 mm long, 147 mm wide, and 0.88 mm thick. The stiffener is 62 mm wide, each flange 0.88 mm thick, and the blade section is 1.76 mm thick. The overall thickness of the specimen from bottom of skin to top of blade is 31.8 mm. A photo of the specimen is shown in Figure 2.2.2.

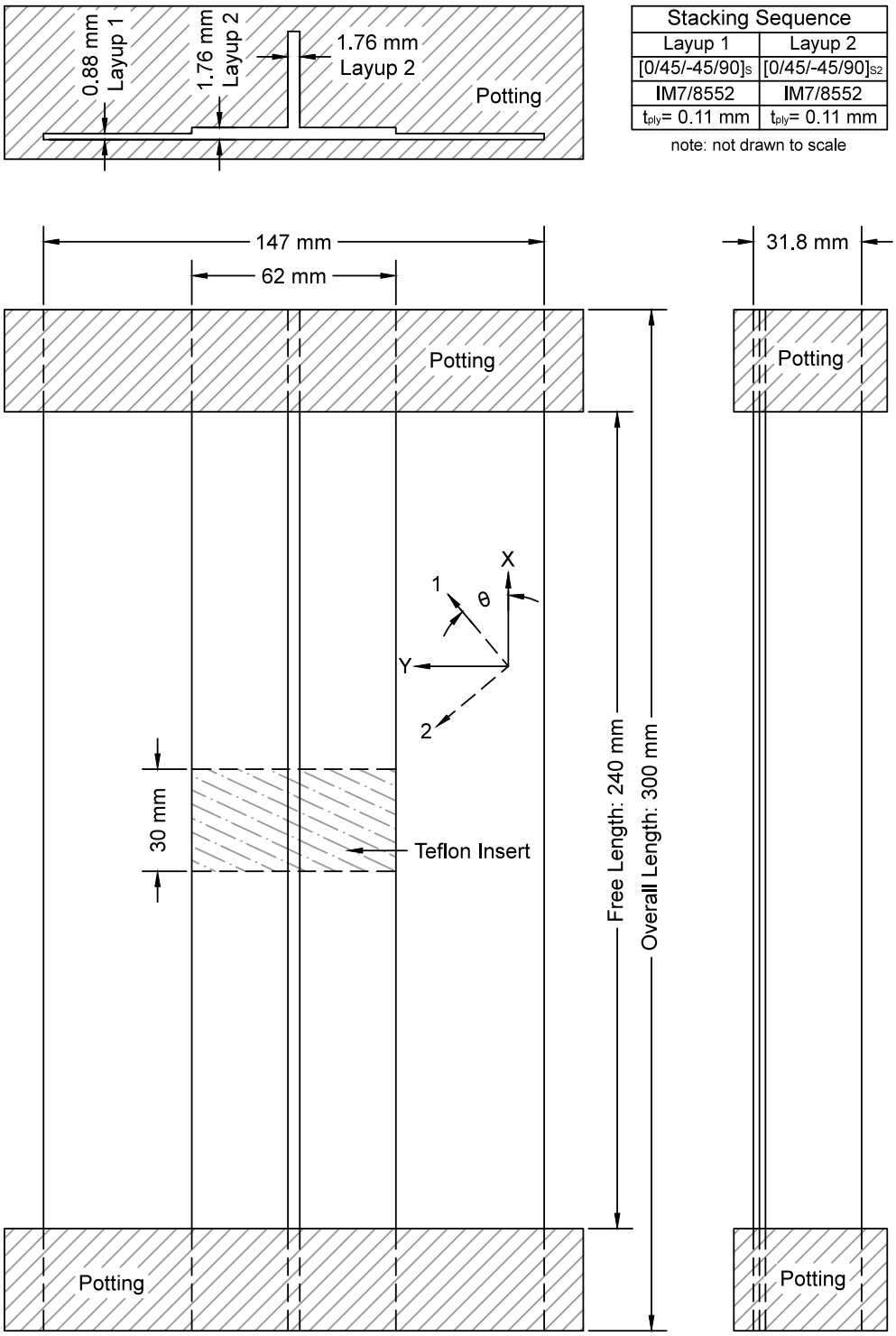

Figure 2.2.1: Specimen SP-1 dimensions

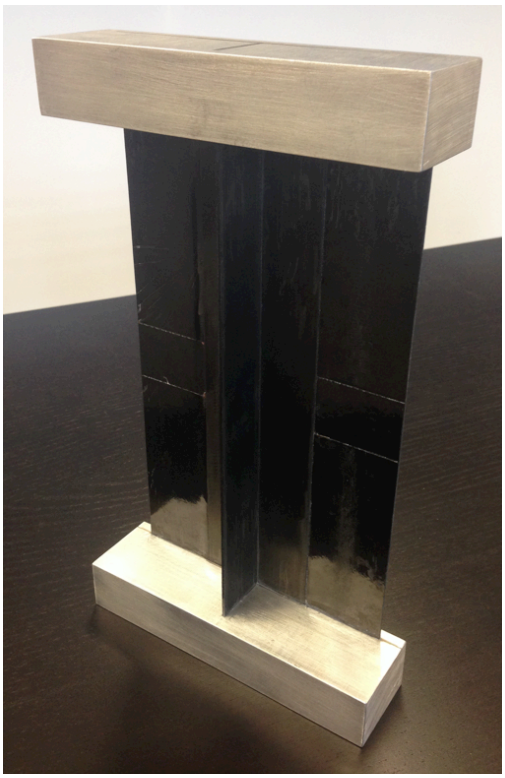

Figure 2.2.2: Specimen SP-1

2.3 - SP-2 Panel

The second panel tested was nominally identical to the first. The difference between the panels was a measured skin thickness of 0.92 mm (4% thicker than SP-1) and a blade thickness of 1.8 mm (2% thicker than SP-1). The difference in thicknesses may be attributed to higher compaction in SP-1 during the autoclave cure.

Chapter 3 - Numerical Modeling

3.1 - Baseline Model

The baseline finite-element model was analyzed in Abaqus/CAE 6.13. This model consisted of a single-shell model 240 mm length with no separation between the skin and stiffener. The consistent units for the model were length: mm, force: N, stress: MPa, time: s, density: tonne/mm^3 and energy: mJ.

The model was comprised of an extruded T-section, 240 mm long. The T-section is 147 mm wide, with the stiffener in the center 31 mm tall. The skin was split at 2 locations (62 mm apart), which allowed two separate composite layup definitions to be used for the skin only section and the skin-stringer flange section. The root of the blade and the flange section of the stiffener did have overlap in the finite-element model. This accounted for less than 1% additional cross-sectional area, and was considered negligible.

A total of three separate composite layups were used in the model. The first was the skin-only section, defined as an 8-ply, $[0/45/-45/90]_S$ layup, assigned with an offset ratio of 0 (middle of section). The skin and stiffener flange region composite layup was a 16-ply, $[0/45/-45/90]_{S2}$ assigned with an offset ratio of -0.25, which aligned the plies within the skin to be continuous throughout. The stiffener blade section was assigned a layup similar to section 2, but oriented within the plane of the blade. Each ply, within the different layups, was assigned a thickness of 0.11 mm, with three integration points per ply. The thickness was integrated according to

Simpsons Rule. The material assigned to the composite layups was Hexcel IM7/8552 with properties given in Table 2.1.1. The shear moduli G_{12}, G_{13}, and G_{23} were considered to be the same. The moduli of the lamina were considered linear to failure.

The model was discretized into 3 mm S4R (4-node quadrilateral) shell elements. There were 4,620 total elements and 4,779 total nodes in the model, as shown in Figure 3.1.1. Two reference points were used to directly apply the loads and boundary conditions. The reference points were located at each end of the specimen, at the centroid of the cross-section. The reference points were constrained to the respective edge nodes of the specimen using ties, which couples all degrees of freedom. The boundary condition of one end of the panel was specified as fixed, while the other end only allowed axial shortening of the specimen. The edge nodes of the skin were left as unconstrained.

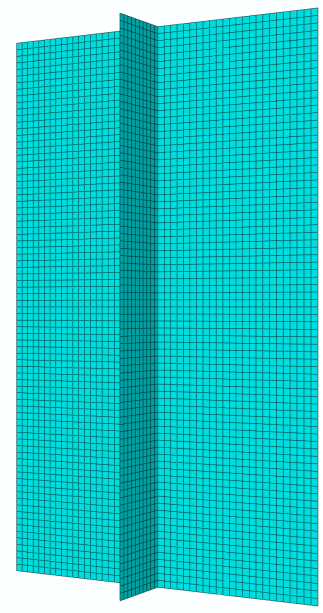

Figure 3.1.1: 3 mm finite element mesh

The first analysis was a linear perturbation, buckling eigenvalue analysis. The analysis included a 1 N compression force to the roller reference node. The analysis captured the first 4 buckling mode shapes and the corresponding buckling load. A second analysis used an applied displacement of 1 mm rather than a force of 1 N and produced an eigenvalue equal to the displacement applied to produce each mode shape. The output requests for each analysis were Field Output U, and UR, of the entire model. Additionally, the node displacements U for each mode shape were saved in a .fil file to input into a subsequent nonlinear model as an initial imperfection shape.

Table 3.1.1: Baseline model buckling values

Mode	Force (N)	Displ. (mm)
1	4047.5	0.069
2	4731.1	0.082
3	5354.9	0.093
4	5926.9	0.102

The buckling values given in Table 3.1.1 are shown in Figure 3.1.2, as well as the linear force-displacement response. The stiffness of the specimen is taken as the slope of the force-displacement curve. From the analysis, this is 58.66 kN/mm. Classical lamination and beam theory predicts the stiffness as k=EA/L. E is taken as the equivalent longitudinal modulus E_x, A is the total cross sectional area of the specimen, and L is the length. k is calculated to be 56.58 kN/mm. The finite element model provides a stiffness 3.7% higher than the theoretical stiffness, which is to be expected as finite element modeling adds stiffness to a structure by imposing a finite number of degrees of freedom.

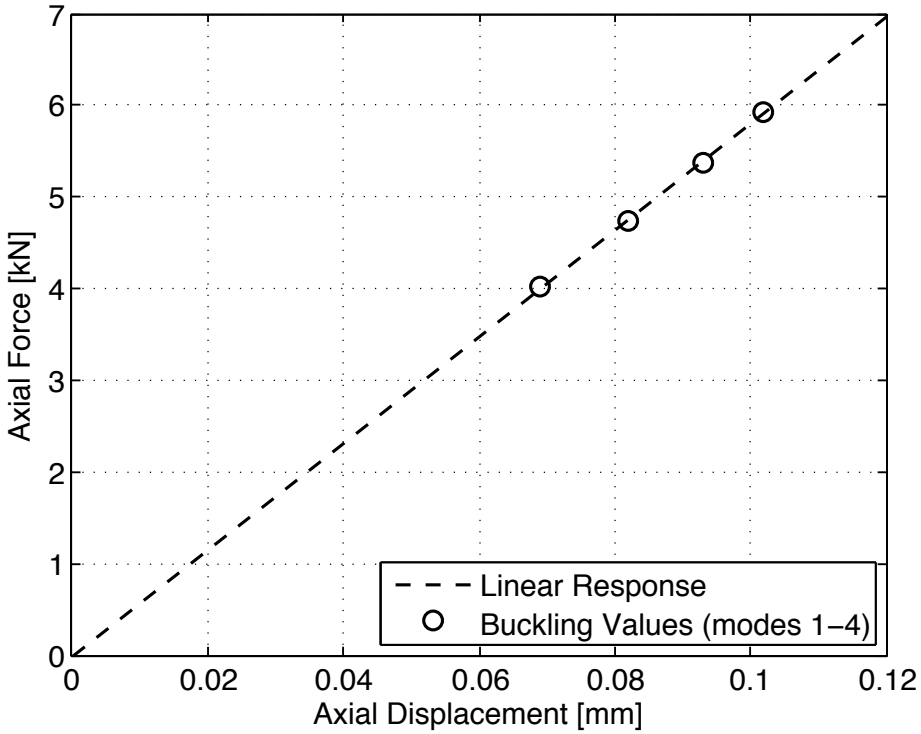

Figure 3.1.2: Linear response of baseline model

The first 4 mode shapes given from the linear perturbation buckling analysis are shown in Figure 3.1.3 to Figure 3.1.6. Note the output of the analysis yields only a 1 mm amplitude of the out-of-plane displacement of the mode shape, and does not consider axial shortening of the specimen. The first mode shape is characterized by single, half-sine waves on each side of the skin, buckled in opposite directions. The second mode shape shows a half-sine wave profile on each side of the skin in opposite directions. The third shape is visually similar to the second, however the skin buckles to the same side. The fourth mode shape is depicted with 3, half-sine wave shapes on each side with both sides acting in the same direction, though the central wave is shown to be larger.

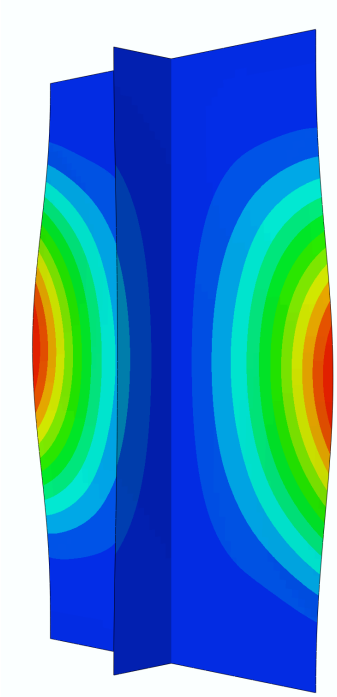

Figure 3.1.3: Mode 1 shape

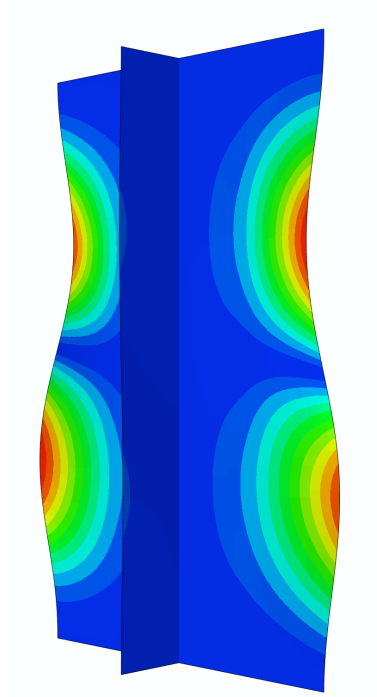

Figure 3.1.4: Mode 2 shape

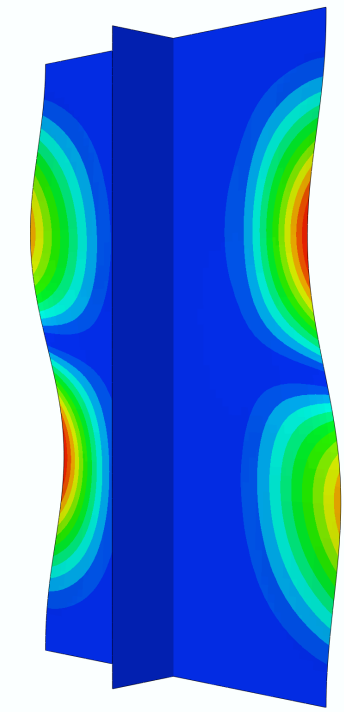

Figure 3.1.5: Mode 3 shape

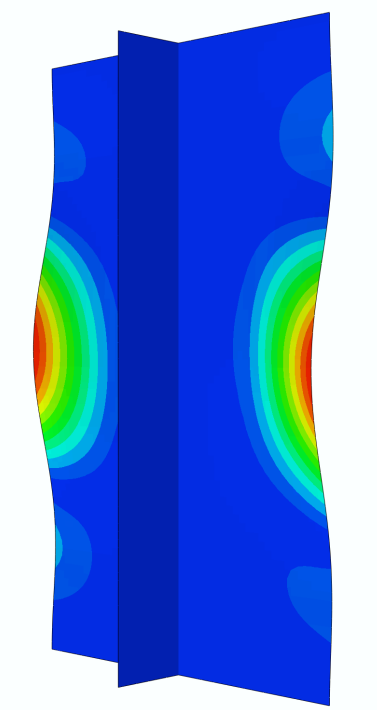

Figure 3.1.6: Mode 4 shape

The second analysis of the baseline model was a static, nonlinear analysis. This type of analysis was required to capture the out-of-plane displacements as well as force-displacement curve throughout the postbuckling of the panel. The analysis solver used was a Full Newton, direct method solver. The panel was loaded in displacement increments of 0.001 mm, to a final displacement of 1.4 mm. In order to initiate buckling behavior in the specimen, an imperfection was included in the model. The first imperfection incorporated into the model was the 1st mode shape from the linear perturbation analysis step, applied to have a maximum magnitude of 0.05 mm. Including the imperfection allowed the model to buckle, as well as convergence of the solution in the postbuckling range.

In addition to the buckling of the panel, the lamina failure strengths were included in the model. These failure strengths were used in order to determine the first ply failure of the panel, according to typical composite failure criteria. The failure criteria used were: Maximum Stress Theory, Maximum Strain Theory, Tsai-Hill Failure Criterion, and Hashin Failure Criterion.

While the Maximum Stress and Strain Theories are non-interactive, meaning there is no considered effect of strength under biaxial loading, the Tsai-Hill and Hashin theories do consider full or partial interaction. The Maximum Stress and Strain Theories included in Abaqus yield only whether failure has occurred without specifying the type of failure. The Tsai-Hill Failure Criterion considers the overall strain energy of an infinitesimal representative-volume-element, and similarly outputs only whether failure has occurred. The Hashin Failure Criterion considers fiber failure

separate from matrix failure, and has the capability to output the failure type as well as occurrence. Because of this capability, the Hashin Criterion is well suited for understanding the failure.

The output requests for this analysis step were field output including displacement, applied force, stress and strain principal components, and failure margin of safety for each failure criteria. The requested history output for each analysis step was the applied force, and axial displacement of the roller reference point.

The general nonlinear analysis, with force-displacement output shown in Figure 3.1.7, shows a decrease in the specimen stiffness after the initial buckle, which is an expected characteristic of postbuckling. The force-displacement curve from the nonlinear analysis closely follows the linear analysis to the point of buckling, and subsequently began to diverge.

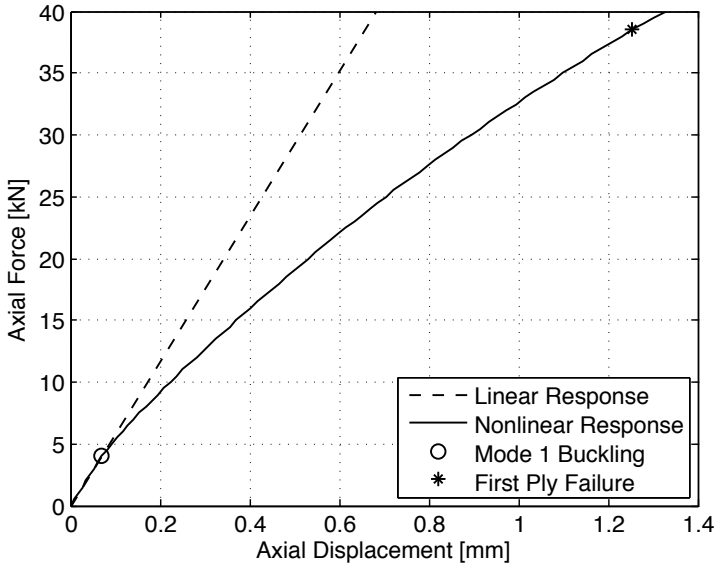

Figure 3.1.7: Nonlinear force-displacement response

The buckling point on the nonlinear force-displacement curve was not apparent because the curve is relatively smooth. One method for determining the onset of buckling from the nonlinear force-displacement data is to analyze the derivatives of the data, shown in Figure 3.1.8. At a displacement value of approximately 0.06 mm, there is an apparent drop in the derivative curve. Since the derivative curve is analogous to the stiffness of the specimen, this corresponds to a significant drop in stiffness of the specimen, which implies buckling. A second derivative of the force-displacement curve yielded the location of the maximum change in stiffness of the specimen, which was the theoretical point of buckling. The maximum in the 2nd derivative curve corresponds to an axial displacement of 0.0671 mm and a force of 3,850 N. This is approximately 5% lower than the buckling force predicted by the linear eigenvalue analysis.

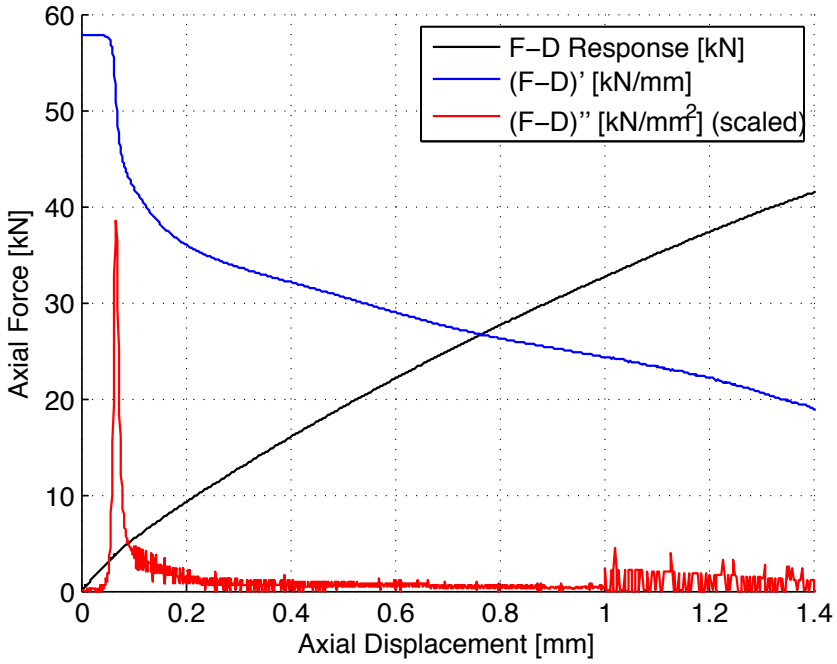

Figure 3.1.8: Determination of buckling point

Beyond the point of buckling, the panel was able to maintain a significant increase in load. The different failure theories predicted very similar failure loads, as shown in Table 3.1.2. The Hashin Failure Criterion, which was most conservative, predicted the first-ply failure to be at a load of 38,628 N, located on the 0-degree ply, opposite the stiffener, in fiber compression. The failure load was approximately 8.5 times greater than the buckling load. The failure occurred at the center of the panel, at the location of maximum curvature, shown in Figures 3.1.9 and 3.1.10.

Table 3.1.2: First ply failure predictions

Failure Theory	Failure Load (N)	Location
Max. Stress	38,630	Ply 1 skin, opposite side of stiffener
Max. Strain	38,675	Ply 1 skin, opposite side of stiffener
Tsai - Hill	38,670	Ply 1 skin, opposite side of stiffener
Hashin		
Fiber Compression	38,628	Ply 1 skin, opposite side of stiffener
Matrix Tension	72,353	Ply 2 skin, middle
Matrix Compression	92,783	Ply 4 skin, middle
Fiber Tension	724,729	Ply 1 skin, corner

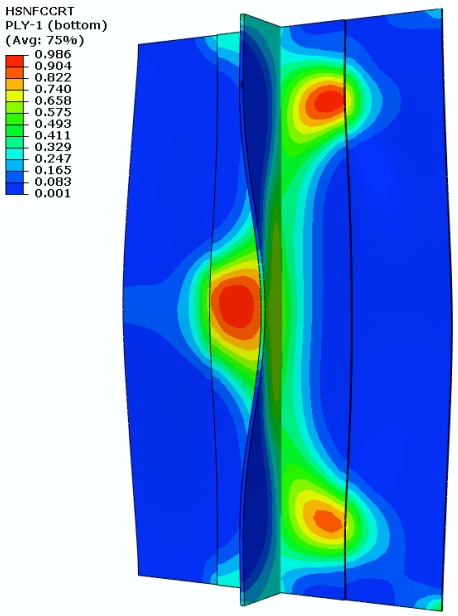

Figure 3.1.9: Hashin fiber-compression bottom (front)

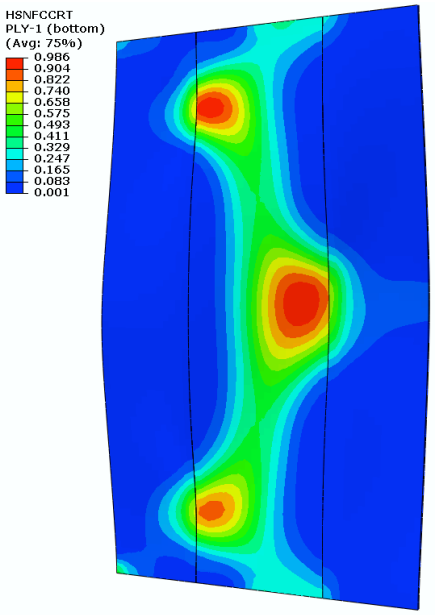

Figure 3.1.10: Hashin fiber-compression bottom (back)

The out-of-plane displacement of the specimen was 13 mm under the failure load, shown in Figure 3.1.11. Compared to the thickness, the out-of-plane displacement of the skin was an order of magnitude larger. This shows the magnitude of the nonlinearity of the specimen. The postbuckled configuration is very similar to the first predicted mode shape from the eigenvalue analysis.

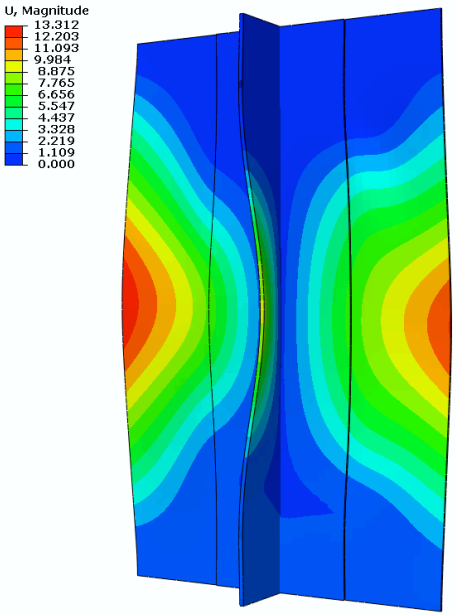

Figure 3.1.11: Out-of-plane displacement (front)

In addition to out-of-plane displacement, the amount of torsion on the buckled panel is noteworthy. After the initial buckle, the middle of the specimen exhibited a large, almost rigid-body, rotation. At the onset of failure, the maximum rotation is exhibited at the center of the stringer at a value of 17º (0.3 rad). The skin however, tends to rotate less than the skin-stringer section. This is shown below in Figure 3.1.12 and Figure 3.1.13.

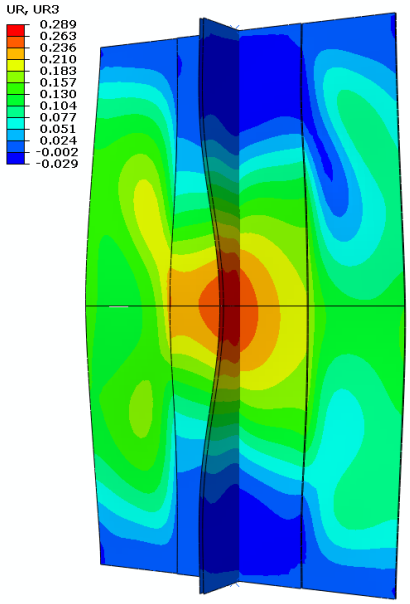

Figure 3.1.12: Axial rotation (front)

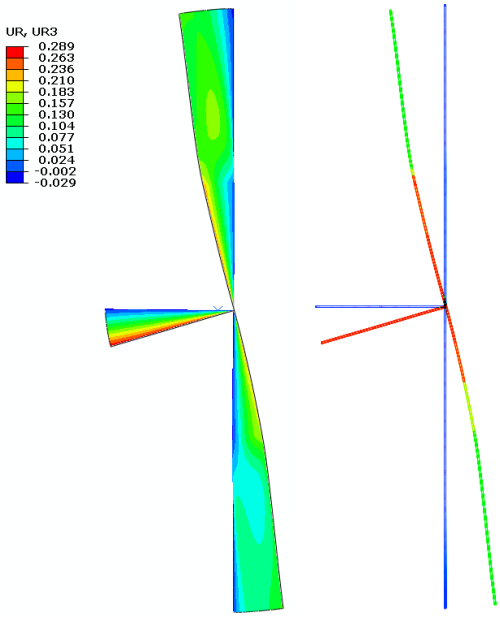

Figure 3.1.13: Axial rotation (top view)

In order to understand the sensitivity of the baseline model to the parameters contained within it, a parametric study was conducted.

3.2 - Model 2: Imperfection Amplitude

This model was used to determine the sensitivity of the panel to larger imperfections. Instead of an initial imperfection with an amplitude of 0.05 mm applied to the model a 0.1 and 1 mm imperfection amplitude was used in separate analyses. No other parameters were changed from the baseline configuration within this model.

Force-displacement curves from each analysis are shown in Figure 3.2.1 and 3.2.2. Figure 3.2.1 zooms in to show the initial segment of the curves, highlighting the slight variation in each model. The onset of buckling from each curve was again calculated using the 2nd derivative. The 0.5 mm imperfection buckled at a force 5%

lower than the 0.05 mm imperfection panel, while the 1 mm imperfection panel buckled at a force 9% lower than the 0.05 mm imperfection panel. Figure 3.2.2 shows the force-displacement curve up to the predicted failure load. The curves from each model nearly overlap, implying the imperfection amplitude does not lead to a significant change in result within the postbuckled range.

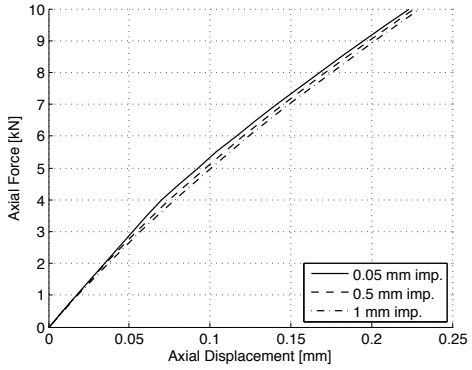

Figure 3.2.1: Initial imperfection amplitude effect

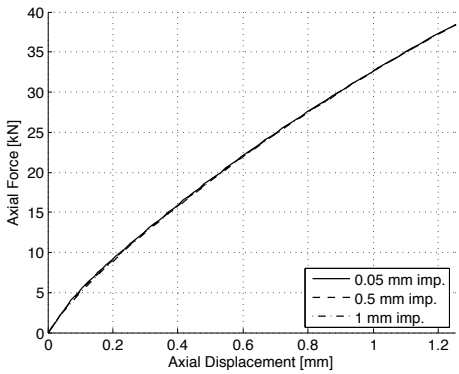

Figure 3.2.2: Overall imperfection amplitude effect

3.3 - Model 3: Imperfection Mode Shape

Model 3 was a study of the influence of the mode shape implemented within the model. This model was created to determine the postbuckling characteristics of each mode shape imperfection within the panel. An imperfection amplitude of 0.05 mm was used within each analysis to remain consistent with the baseline. The analyses were implemented with imperfections of modes 2, 3, and 4 separately, which were taken from the linear eigenvalue analysis. Due to the expected mode shape change, a Riks Arc-Length Method analysis was used, but proved to be ineffective since the mode shape changes were severe. To maintain convergence of the solution, a dynamic analysis was used to capture the mode switch. The dynamic analysis

included an implicit solver, applying incremental displacement to the specimen quasi-statically.

The output from the model, given in Figure 3.3.1, displayed a significant change in the force-displacement response of the panel to the different mode shapes. As expected, the higher mode shapes showed a stiffer force-displacement response. At approximately 0.5 mm displacement, the postbuckled shape from the mode 1 and mode 2 analyses have the same force value. However, the postbuckling response of mode 2 is less stiff than the mode 1 response. The first-ply failure prediction from the mode-2 analysis (shown by the asterisk on the curves) is at approximately the same force level as mode 1, but at a slightly larger axial displacement. The failure type was predicted to be fiber compression in the bottom layer of the skin, at the maximum of the buckle, based on the Hashin Failure Criterion.

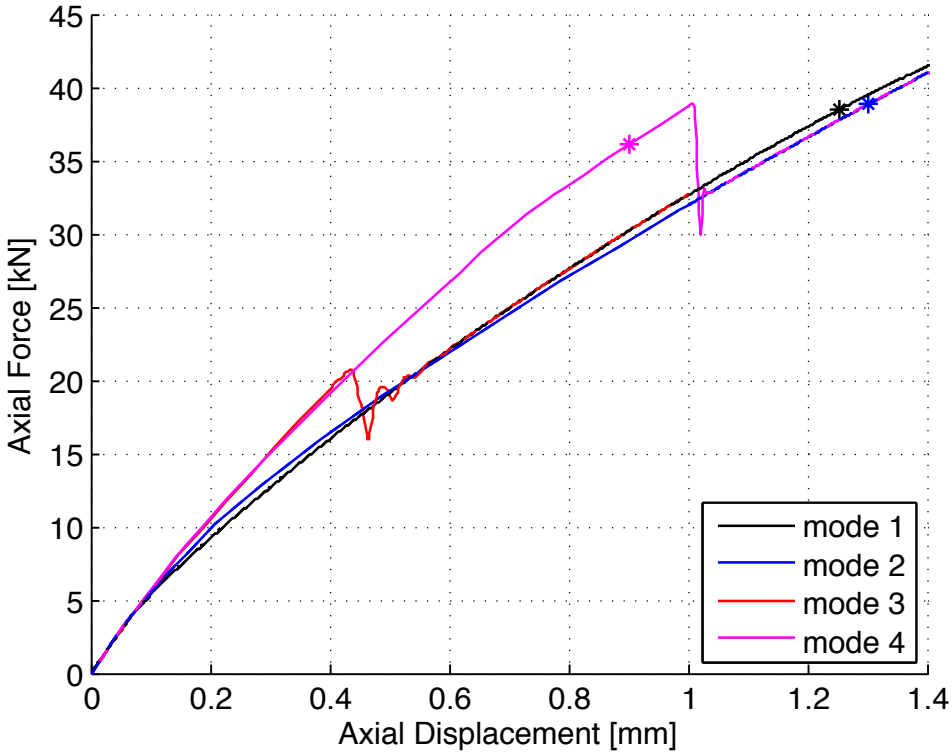

Figure 3.3.1: Postbuckling response for each mode shape

Neither the Newton solver, nor the Arc-length solver was able to converge past a certain point for the mode 3 and mode 4 analyses, which suggested a mode switch. This mode switching could not be captured in a static analysis because of the dynamic characteristics of the mode switch. In order to determine the subsequent mode shapes, an implicit dynamic analysis was implemented after the static analysis reached a displacement of 0.4 mm for mode 3, and 1 mm for mode 4. The displacements beyond this point were then applied at a rate of 0.02 mm/s.

The mode 3 analysis exhibited a switch to match a mode 1 postbuckling configuration at an axial displacement of 0.45 mm. The mode switch increased the magnitude of the buckle in 2 opposite diagonal half-sine waves, as it simultaneously reduced the other half-sine waves to zero. The panel was left with the single half-sine

wave on either side of the specimen. The progression of mode switching is shown below in Figure 3.3.2 to Figure 3.3.4, note the scale of the color spectrum is not the same within each figure.

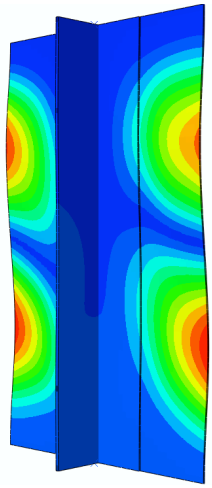

Figure 3.3.2: Mode 3 (0.434 mm axial displacement)

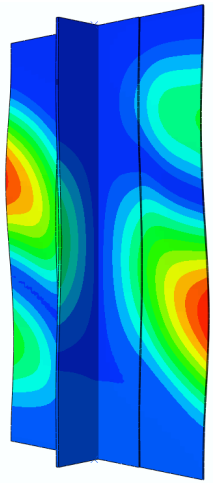

Figure 3.3.3: Mode 1 & 3 mixed (0.449 mm axial displacement)

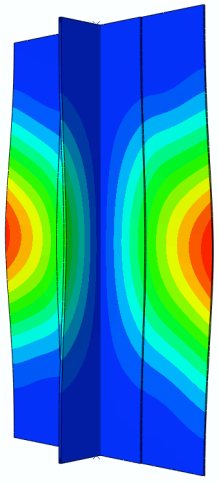

Figure 3.3.4: Mode 1 (0.464 mm axial displacement)

The mode 4 analysis exhibited a mode switch to mode 2 at 1 mm axial displacement; however, the first-ply failure was determined to occur before the mode switch to exhibit a mode 2 configuration. The failure location was also in a different location than given in the mode 1 and mode 2 analyses. The procession of mode shape change from mode 4 to mode 2 is shown in Figure 3.3.5 to 3.3.7. The top left and bottom right half-sine waves increased in magnitude, as well as the middle half-sine waves, which progresses more to the ends. The top right and bottom left half-sine waves were reduced to zero.

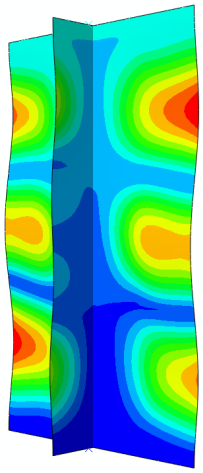

Figure 3.3.5: Mode 4 (1.010 mm axial displacement)

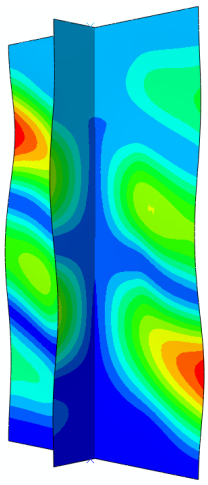

Figure 3.3.6: Mode 2 & 4 mixed (1.015 mm axial displacement)

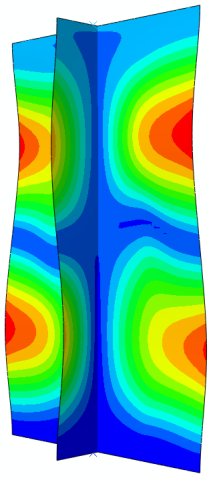

Figure 3.3.7: Mode 2 (1.021 mm axial displacement)

The analyses showed the mode 1, mode 2, and mode 4 initial imperfection shapes were stable to the point of failure, but mode 1 and mode 2 showed a very similar force-displacement response, significantly less than that given by mode 4. Because of this, mode 1 and 2 are expected to be more critical when loading the specimen into the postbuckling range.

3.4 - Model 4: Mixed Mode Shape Combinations

Mode 1 and 2 were determined to be the critical modes as shown in model 3. A subsequent model was created to study the influence of the initial presence of both modes in the postbuckling range. The buckled shape of the panel in a static configuration can exist only as one discrete mode and will tend to buckle according to the dominant mode. The dominant mode was most likely to be present in the test specimens. The combinations of modes and corresponding amplitudes used are shown in Table 3.4.1.

Table 3.4.1: Mode imperfection amplitude combinations

Imperfection Amplitude		Postbuckling
Mode 1	Mode 2	Mode Shape
0.05	0	1
0.05	0.05	1
0.05	0.1	1
0.05	0.25	1
0.05	0.5	1
0.05	1	2
0	0.05	2

The model showed the tendency of buckling and postbuckling to occur in the first mode configuration. In order to induce postbuckling in the mode 2 configuration, with both mode 1 and 2 imperfections applied, mode 2 required an imperfection amplitude 20 times greater than mode 1 imperfection. This suggested mode 1 was the more critical postbuckling configuration.

3.5 - Model 5: Specimen Length

The baseline model considered the length of the specimen to be 240 mm, with fixed boundary conditions, which corresponds to the free length of the panel. However, the actual panel is adhered to aluminum potting, which is not an ideal, clamped boundary condition. Considering the effective length of the panel to be longer, could give a more accurate representation of the potting. The effective length of the specimen in model 5 was adjusted to 270 mm, and 300 mm. These lengths were consistent with the center-to-center measurement of the tabs and the overall length of the specimen, respectively.

The length of the specimen was shown to have significant influence on the force-displacement response of the panel, shown in Figure 3.5.1. As expected, the shorter panel is the stiffest, and the longer panel is the least stiff. Each of the curves shows a similar trend, of a lower buckling load with longer panels and a decrease in stiffness in the postbuckling range.

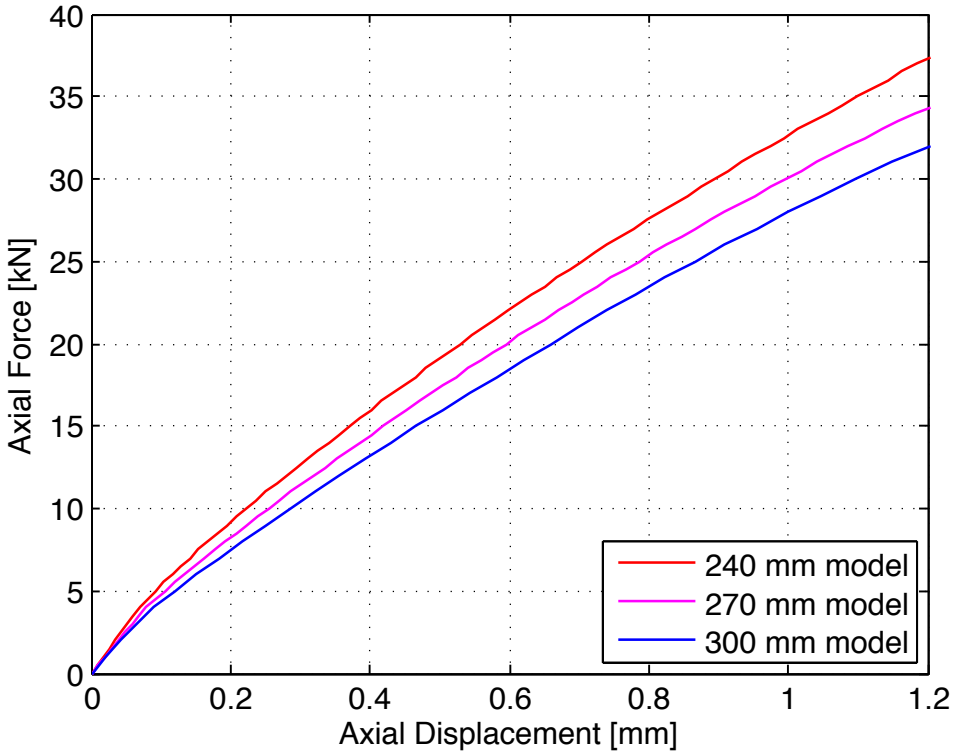

Figure 3.5.1: Influence of panel length

At an axial displacement of 1 mm, the baseline model (240 mm panel) has a reaction force of 32.6 kN. The 270 mm panel has a 30 kN reaction force, 8% lower than the 240 mm panel. The 300 mm panel has a 28 kN reaction force, which is 14% lower than the 240 mm panel.

3.6 - Model 6: Mode Shapes on Long Panel

Because of the significant change in response of the different length panels, the influence of different initial mode shapes were considered in a longer panel. Model 6 investigates the different mode shapes on the 270 mm panel, similar to model 3. The same procedure is used as in model 3. The results are also very similar to model 3, as shown in Figure 3.6.1. The mode 1 and mode 2 response both remained stable to the onset of first-ply failure, while mode 3 and mode 4 switched to modes 1 and 2, respectively. After the switch, the force-displacement curves aligned with the original mode 1 and mode 2 configurations, respectively. Mode 4 switched to mode 2 much earlier than in the 240 mm model, and does not experience first-ply failure in the mode 4 configuration.

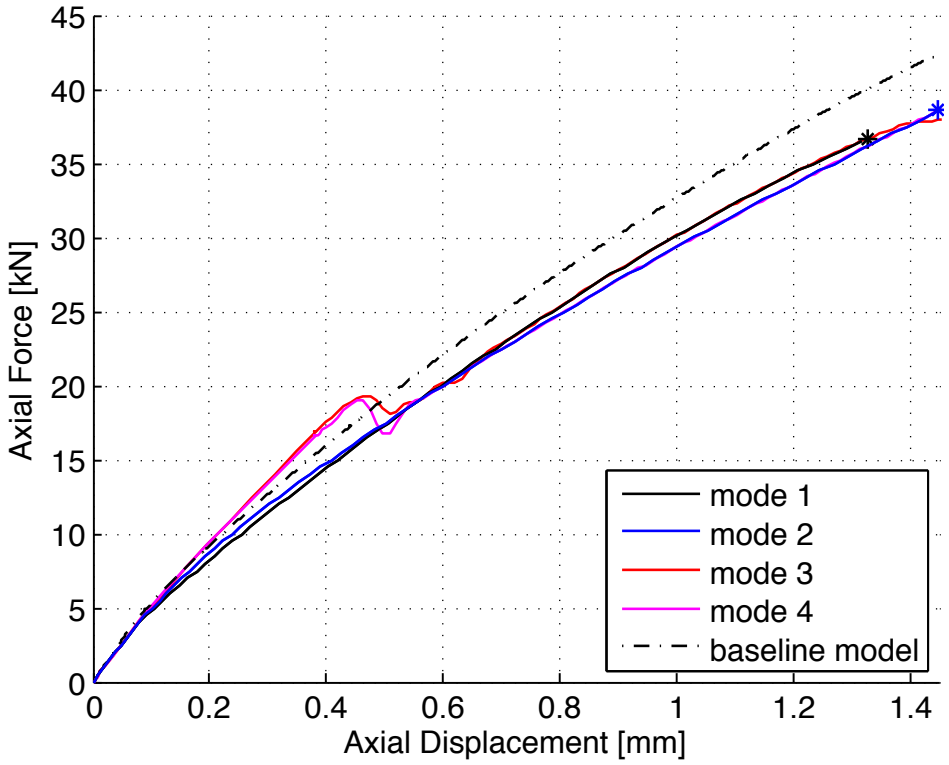

Figure 3.6.1: Postbuckling response for modes 1-4 of 270 mm panel

3.7 - Model 7: Mesh Refinement

Model 7 introduced a mesh refinement to the baseline model. Instead of 3 mm elements, the model used 1.5 mm S4R type elements. This model was used to determine the proper mesh size for modeling the postbuckling response of the panel. This model increases the number of nodes from 4,941 to 19,320. This increase in the number of degrees of freedom within the model led to an 800% increase in computation. The refined mesh model yields a stiffness of approximately 57.85 kN/mm, which is a decrease in stiffness of 1.4% from the baseline model. The nonlinear region of the force-displacement curve differs by less than 1% from the baseline model, as well as the predicted first-ply failure load. Since the difference is small, the 3 mm elements can be regarded as adequate.

3.8 - Model 8: Mode 1 Quasi-Static Response

The baseline model considers the panel under static loading. Since the testing of the panel is done quasi-statically, model 8 considers a quasi-static dynamic implicit analysis. Instead of an applied end displacement, a velocity was applied to the roller reference node at 0.1 mm/s. The time period of the step was 15 seconds, with maximum increments of 0.01 sec. The force-displacement curve is shown below in Figure 3.8.1.

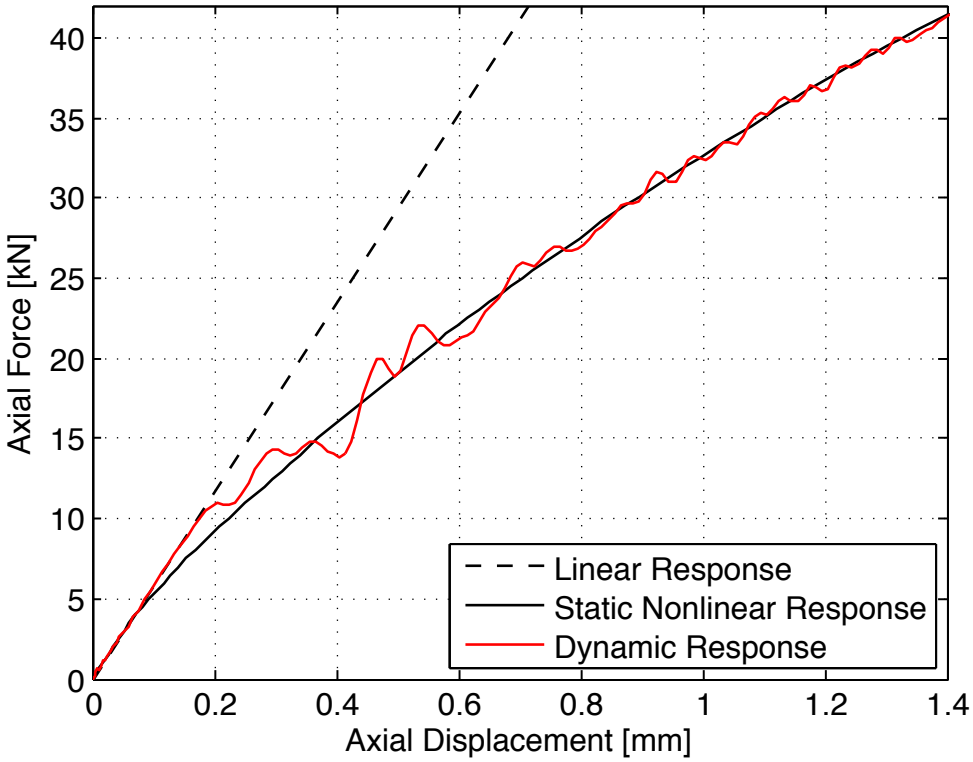

Figure 3.8.1: Dynamic response (0.1 mm/s velocity)

The force-displacement response of the panel shows an initial linear response, which continued to more than twice the buckling load. At a displacement of approximately 0.2 mm, the response deviated from the linear response and continued to follow the static nonlinear analysis response. However, as described by Wullscheger et al. [5] and Bisagni et al. [6] the time step should be decreased especially near the point of buckling.

3.9 - Model 9: Double Shells with Ties

Within the baseline model, the skin and stringer section are defined as a single composite layup, without the Teflon separation between them. In order to include a delamination between the skin and stringer, they must be considered as separate composite layups. Model 9 introduced a separate shell into the model. Including the

shell separately required the two shells to be fixed together using tie constraints at the interface of the skin and stiffener. The tie constraints, which were used over the entire interface, maintained strain-compatibility between the nodes of the shells. The addition of another section of shell elements did increase the number of elements within the model. In all other instances, models 1 and 9 are equal.

Table 3.9.1: Model 9 buckling values

Mode	Force (N)	Displ. (mm)
1	4014.0	0.0699
2	4700.8	0.0818
3	5320.4	0.0926
4	5888.7	0.1025

The results from model 1 and model 9 are nominally identical. The eigenvalue buckling analysis results were within 1% of the baseline model. The mode shapes were also identical to the baseline model. The force-displacement curve, shown in Figure 3.9.1 was slightly lower than the baseline, with the failure load predicted by the Hashin Failure Criteria 1.5% lower than the baseline model. The failure type and location were also the same as the first model. These results indicated no significant difference with modeling the skin and stiffener as two separate layups.

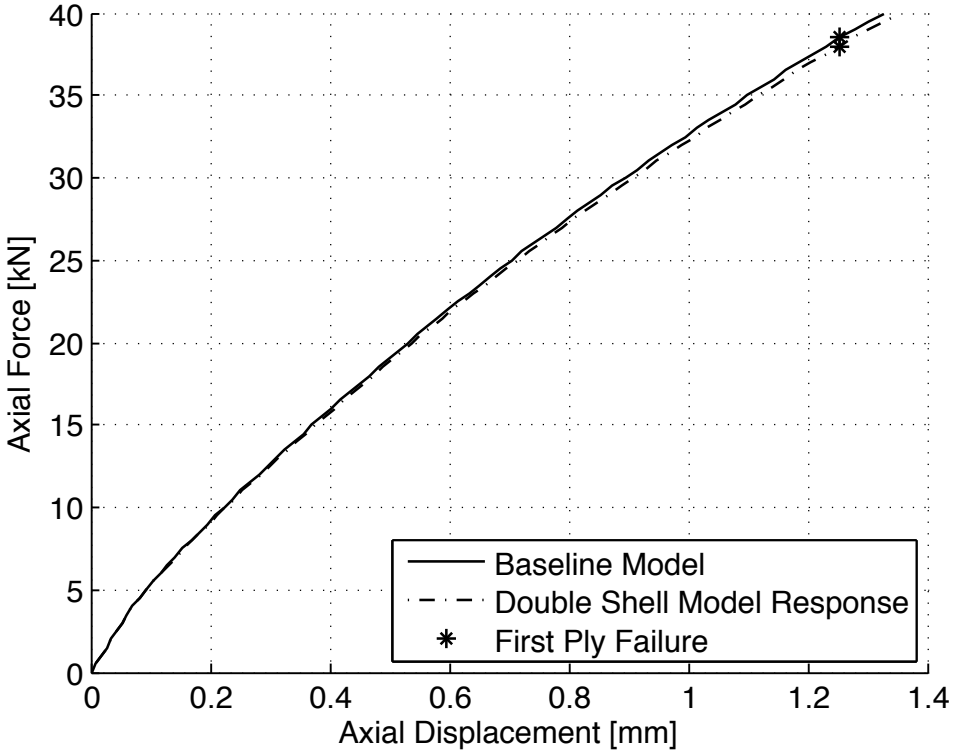

Figure 3.9.1: Influence of tie constraints

3.10 - Model 10: Skin-Stringer Contact

Similar to model 9, model 10 used the separate shell for the stringer and the tie constraints. However, model 10 removed the ties between the skin and stiffener shells of the second model at the location of the Teflon. Instead of a tie, a contact property was used. The normal direction contact property was defined as hard contact, while the tangential direction was set to frictionless. This simulated the panel and stiffener being able to compress against one another without transferring through thickness tensile or shear stress.

The results of this model showed a significant decrease in strength before first-ply failure. The predicted failure load according to the Hashin failure theory is 31,650 N. This is an approximate 18% decrease from the baseline model. The failure

location remains in the same place, and same failure type. The failure location is more concentrated than the models without separation between the skin and stiffener. Though the first-ply failure is significantly lower, the panel only shows a slight decrease in stiffness.

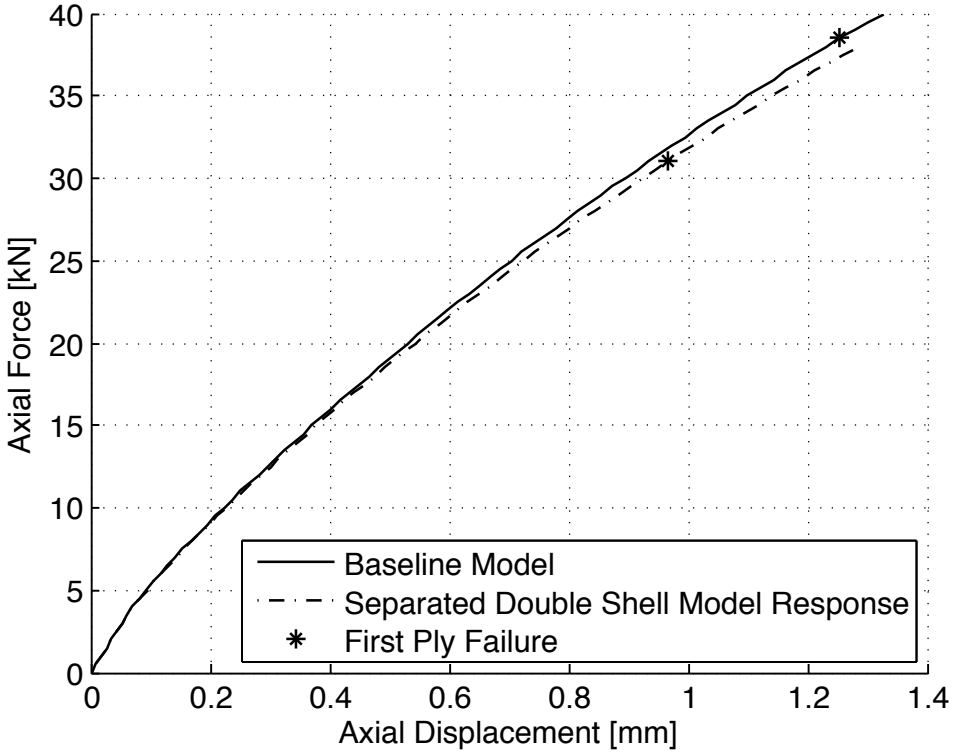

Figure 3.10.1: Influence of Teflon separation in mode 1

The force-displacement response considering the 2nd mode configuration is similar to the 1st mode configuration, which is shown in Figure 3.10.2. The double shell panel with Teflon separation showed slightly more compliance than the model without separation and also yielded a first-ply failure prediction at a load 24% lower than the model without separation. The failure location is predicted as fiber compression damage according to Hashin Criterion at the bottom ply of the stiffener

flange, directly above the edge of the Teflon. This suggests the mode 2 configuration may be more susceptible to the pre-damaged area.

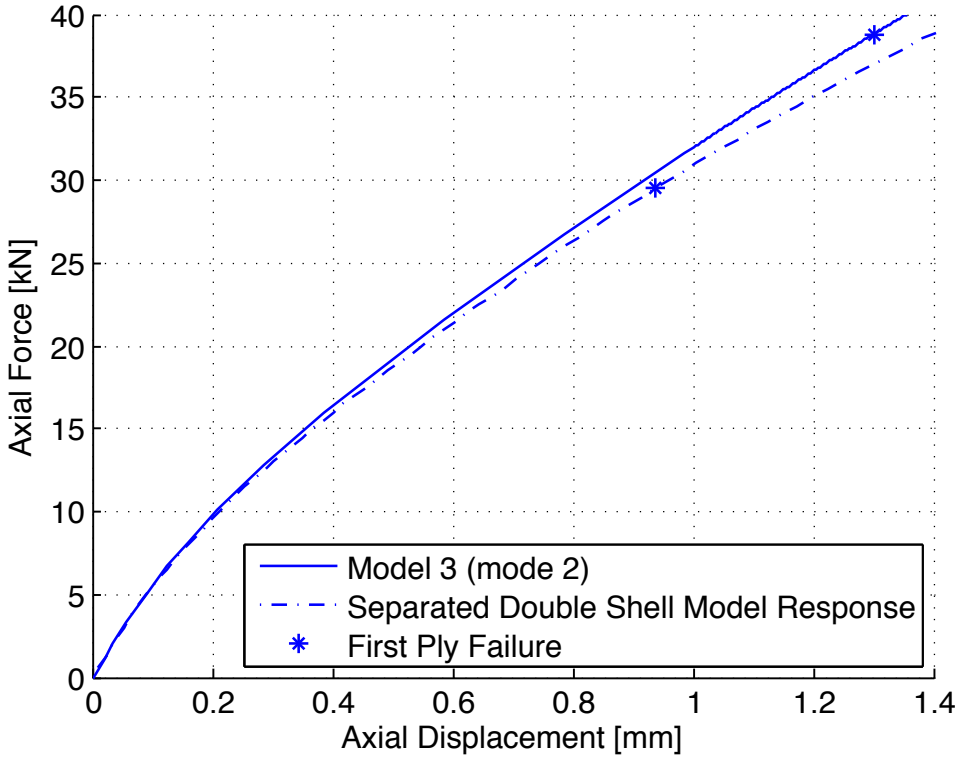

Figure 3.10.2: Influence of Teflon separation in mode 2

Chapter 4 - Experimental Procedure

4.1 - Testing Setup

An experiment was conducted to determine the buckling and postbuckling behavior of the test specimens and validate the numerical analysis. An MTS Landmark servo-hydraulic load frame was used to load the specimen in compression. The load frame allowed for high accuracy force and displacement control, as well as data acquisition. The load frame and the testing setup are shown in Figure 4.1.1, with a description of each component given in Table 4.1.1.

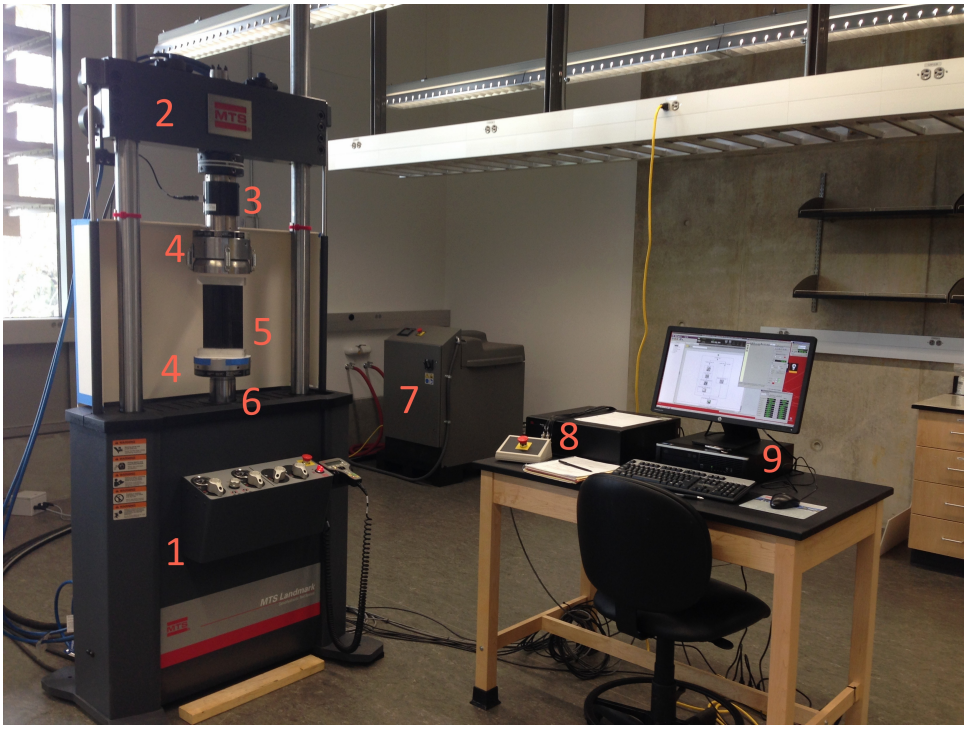

Figure 4.1.1: Testing equipment

Table 4.1.1: Testing equipment description

Number	Description
1	MTS Landmark Servo-Hydraulic Load Frame (250 kN capacity)
2	Crosshead
3	Load Cell
4	Compression Platens (self-leveling)
5	Composite Panel Specimen
6	Hydraulic Actuator & Linear Variable Differential Transducer (LVDT)
7	MTS Hydraulic Power Unit/ Pump
8	MTS FlexTest Digital Controller
9	PC with MTS TestSuite Elite

4.2 - Testing Procedure

The MTS TestSuite program was used to load the panel and serve as the data acquisition. A program template was created before the test to serve as a safety. In order to run the test, the crosshead was fixed in place and the actuator was moved into place. The panel was aligned on the compression platens using the template, shown in Figure 4.2.1 and Figure 4.2.2. The template served to position the centroid of the panel at the center of the platen. The top platen was initially separated from the specimen.

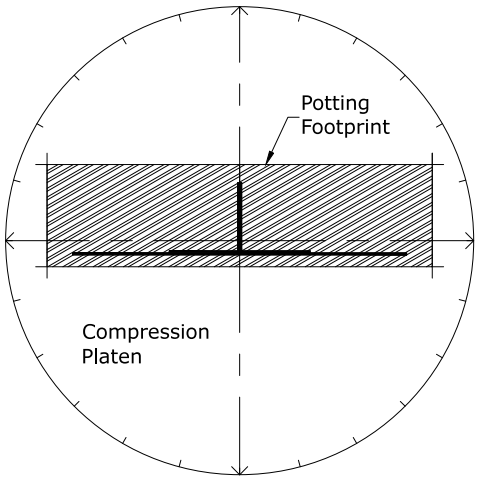

Figure 4.2.1: Placement template

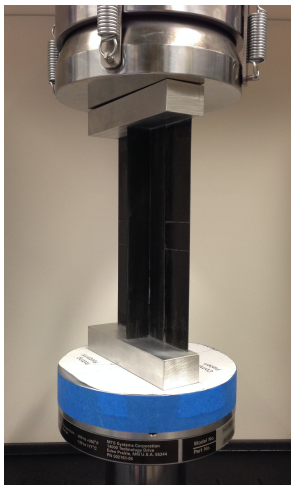

Figure 4.2.2: Specimen on platens

At the beginning of the MTS program, shown in Figure 4.2.3, and 4.2.4, the load cell was set to zero, then the actuator began to move up at a rate of 2 mm/min. Simultaneously, the program recorded the time, load, and displacement data for the entirety of the test. Once a load of 500 N was reached, the program set the displacement to zero, and the actuator stopped, maintaining zero displacement. The program opened a window requesting permission to continue, which if granted, would increment the displacement on the specimen by 0.05 mm. Once the 0.05 mm increment has been reached, the program paused until the continue button was activated. After the desired number of increments had been reached, the stop button was activated, and the load was removed from the panel. The program template is shown in Figure 4.2.3. Pictures were taken at different increments of displacement to show the out-of-plane response at discrete intervals points

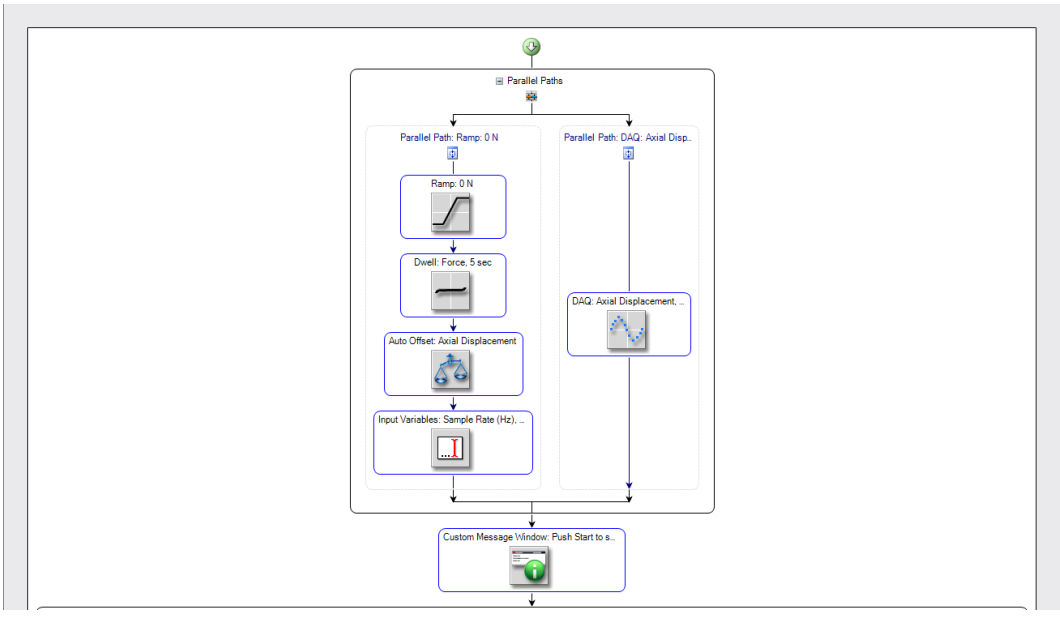

Figure 4.2.3: MTS TestSuite program template (part 1 of 2)

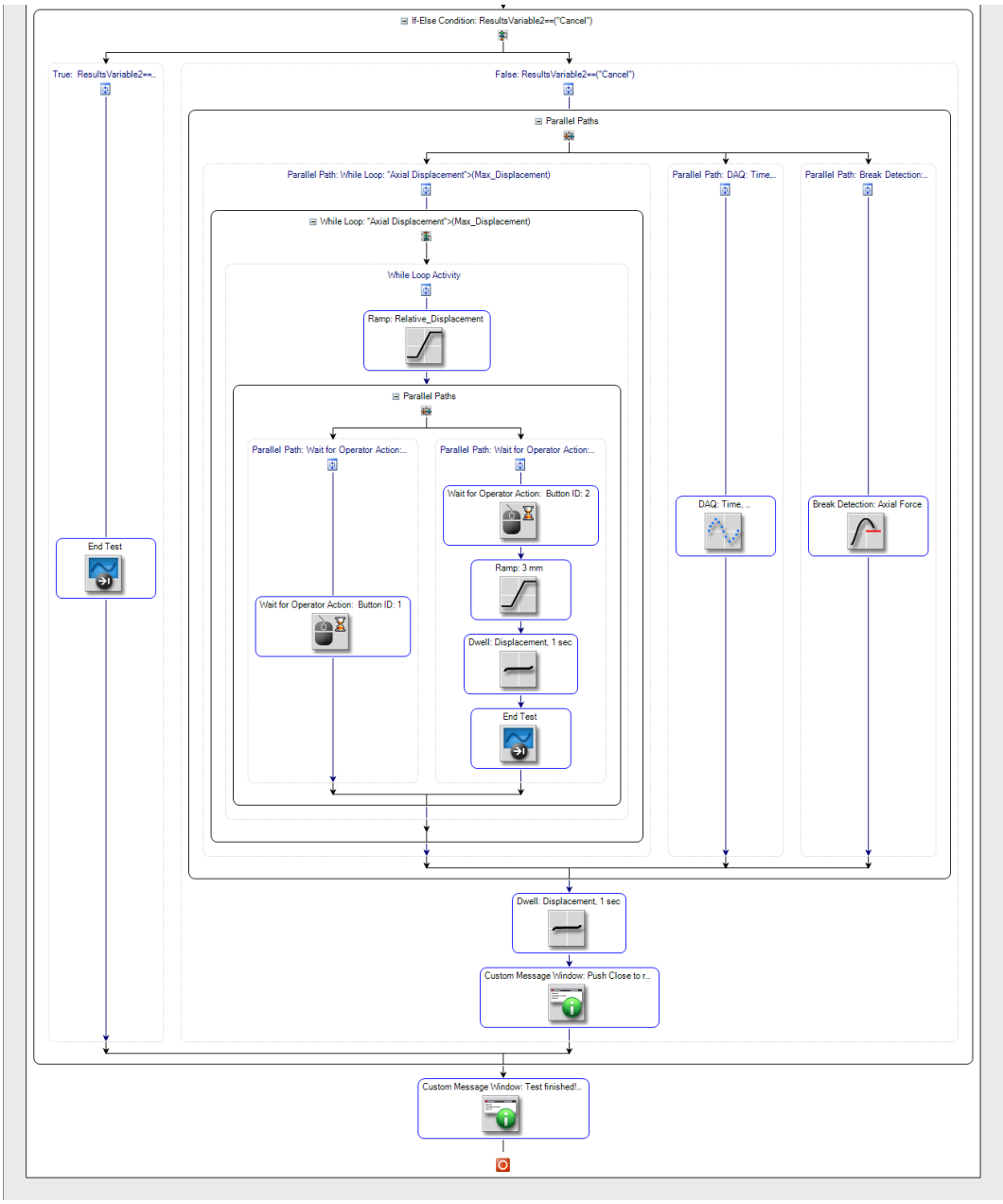

Figure 4.2.4: MTS TestSuite program template (part 2 of 2)

4.3 - Test Results

The specimens SP-1 and SP-2 were loaded several times in displacement control. The response of each specimen remained the same after each time load was applied, proving the specimens remained elastic, and had no degradation. The panels

were loaded to 0.6 mm axial displacement, which resulted in a reaction force of approximately 21 kN. The panels both exhibited the same buckled configuration, with a single, half-sine wave buckle in each side of the skin, as well as the blade section of the stiffener, as shown in Figure 4.3.1. The cross section at the center of both specimens seemed to rigidly twist, maintaining the same cross section. After the load was removed, the specimens returned to the undeformed shape.

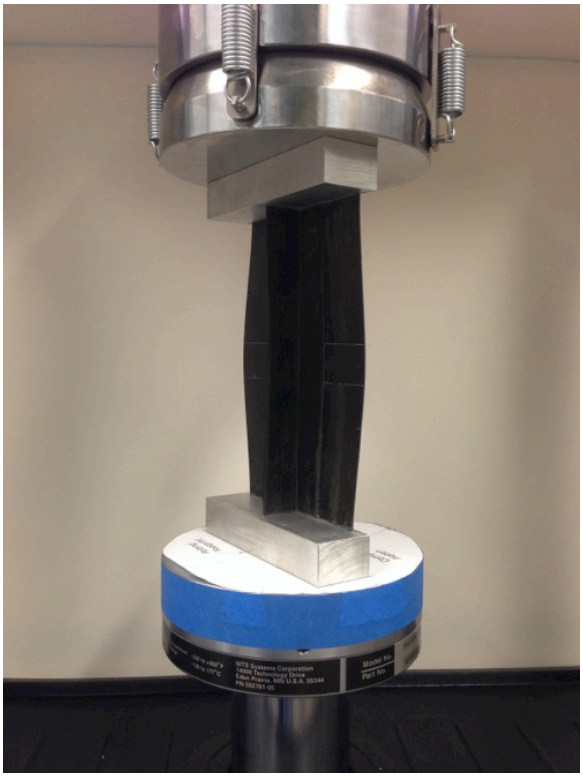

Figure 4.3.1: Specimen SP-1 at 0.6 mm axial displacement

The force-displacement curves from both tests are taken from data output from the MTS TestSuite program, shown in Figure 4.3.2 and 4.3.3. The displacement data was shifted so that the initial, linear segment of the curve would be extrapolated to (0,0), to neglect the system compliance.

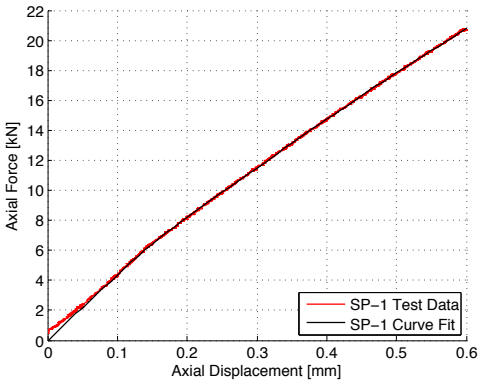

Figure 4.3.2: SP-1 curve-fit

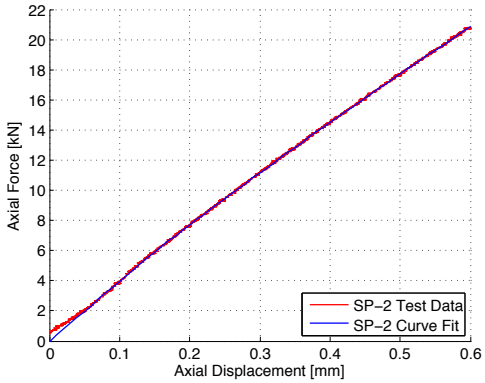

Figure 4.3.3: SP-2 curve-fit

The response from SP-1, shown in Figure 4.3.2 shows an approximately linear response to 6 kN, then a decrease in stiffness beyond this point. The initial, pre-buckled stiffness of SP-1 was calculated to be 43.5 kN/mm. The change in slope of the plot at 6 kN can be attributed to the onset of buckling, however the panel showed gradual out-of-plane deformation to this point. As expected, the postbuckled range shows a decrease in stiffness.

The response from SP-2, shown in Figure 4.3.3, shows a very similar linear trend to 6 kN, as in SP-1. The initial linear segment shows a stiffness of 40 kN/mm, 8% less than SP-1. The point of buckling in SP-2 is less severe, compared to SP-1. The postbuckling range shows an overall stiffness slightly higher than SP-1, as both panels maintained a reaction force of 21 kN at 0.6 mm axial displacement.

The repeated tests on each specimen demonstrated the ability to maintain loads well above the buckling load. Both panels show signs of buckling around 6 kN, but are able to maintain loads of 21 kN without the onset of damage. This proves the

postbuckling capacity of the panels can be at least 3.5 times the buckling load, even with the included Teflon region simulating delamination.

Figures 4.3.4 and 4.3.5 show the front of the panels under different levels of axial displacement. The photographs were taken from the same angle and at the same discrete intervals in the loading process. The photographs show the progression of the postbuckling in the panels. Figures 4.3.6 and 4.3.7 show the back side of the panels under the same loading conditions.

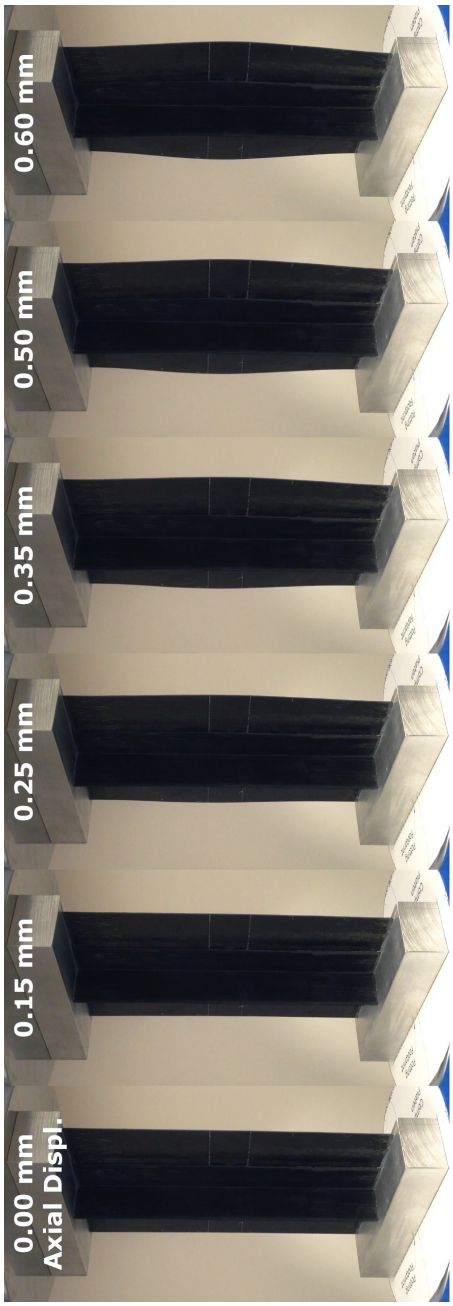

Figure 4.3.4: SP-1 axial displacement increments (front)

Figure 4.3.5: SP-2 axial displacement increments (front)

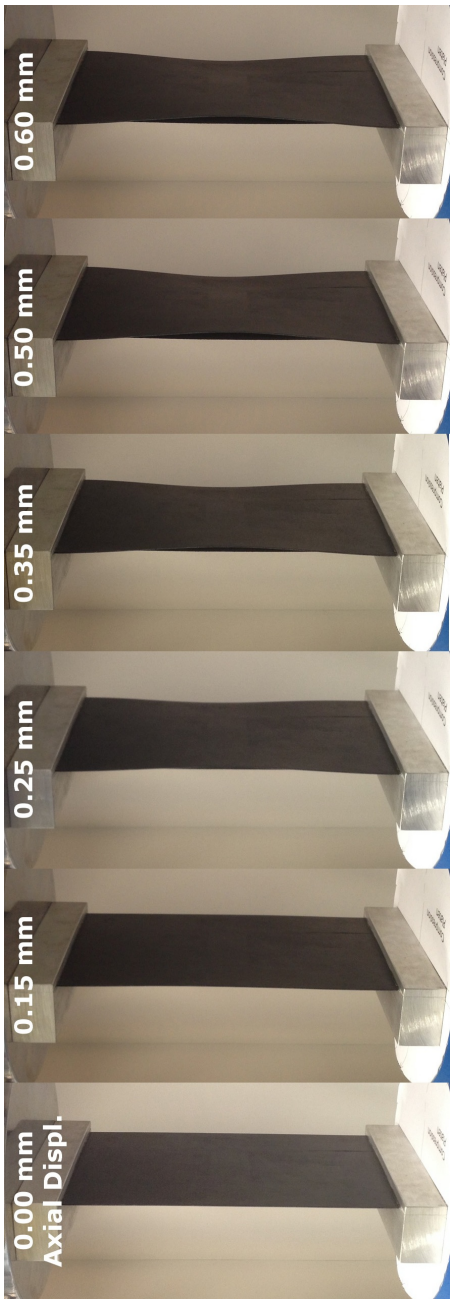

Figure 4.3.6: SP-1 axial displacement increments (back)

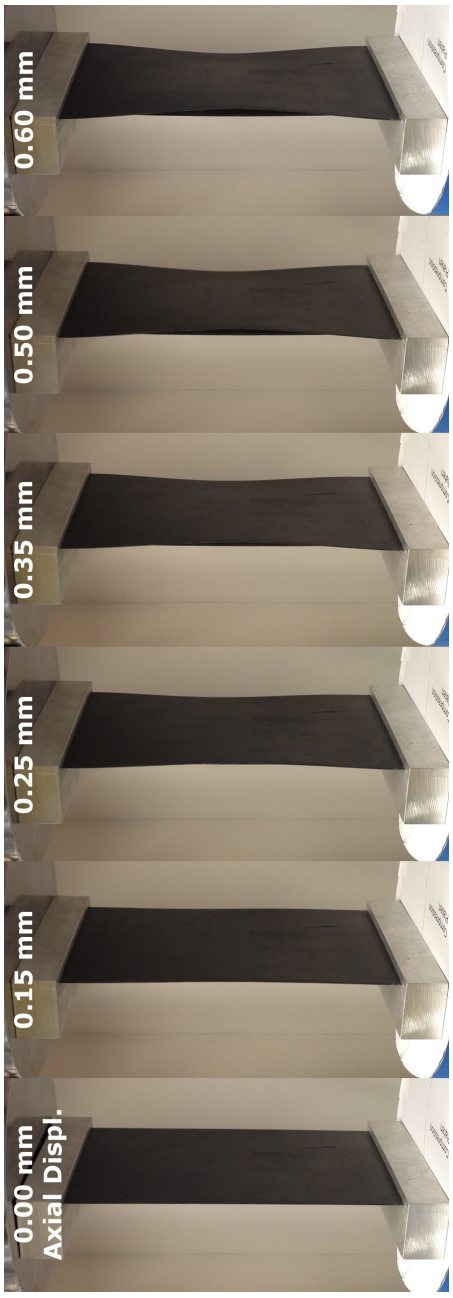

Figure 4.3.7: SP-2 axial displacement increments (back)

The out-of-plane displacement of both panels was measured at various displacement levels to compare with the finite element model. For this, a straight edge was placed next to the specimen and the out-of-plane displacement was measured with a ruler, as shown in Figure 4.3.8. At an applied axial displacement of 0.6 mm, the out-of-plane displacement of the skin was measured to be 8.5 mm for both panels, and the stringer out-of-plane displacement was 4 mm for SP-1 and 3.5 mm for SP-2.

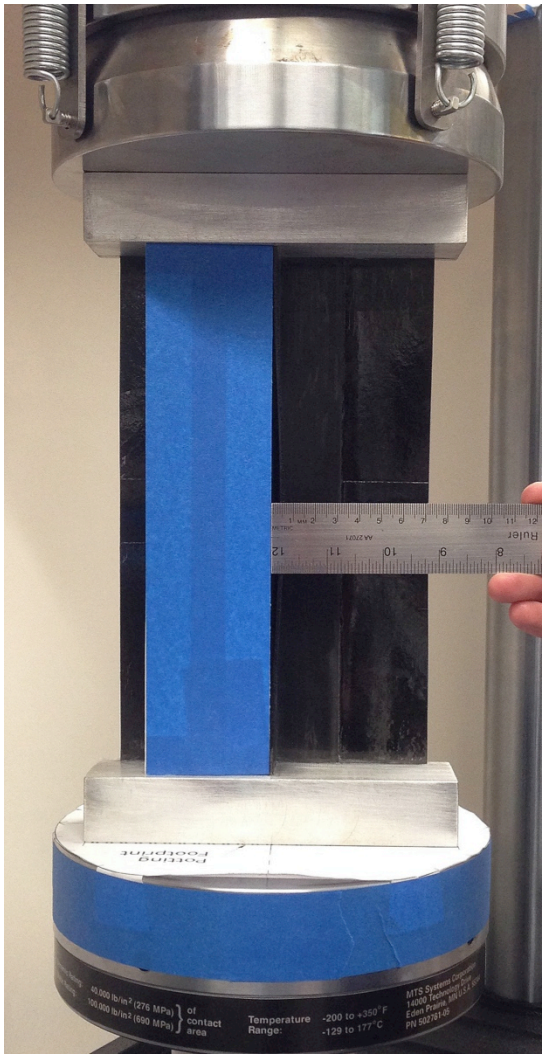

Figure 4.3.8: SP-1 stringer blade displacement under 0.06 mm axial displacement

Chapter 5 - Numerical - Experimental Correlation

5.1 - Numerical - Experimental Comparison

A plot comparing the force-displacement test data to the finite element models is shown below in Figure 5.1.1. The three models displayed include the mode 1, 0.05 mm imperfection, with varying panel lengths. The 240 mm model predicted an initial stiffness of 58.66 kN/mm, 35% stiffer than the SP-1 test, while the 300 mm model predicted an initial stiffness of 46.2 kN/mm, only 6% stiffer than the SP-1 test.

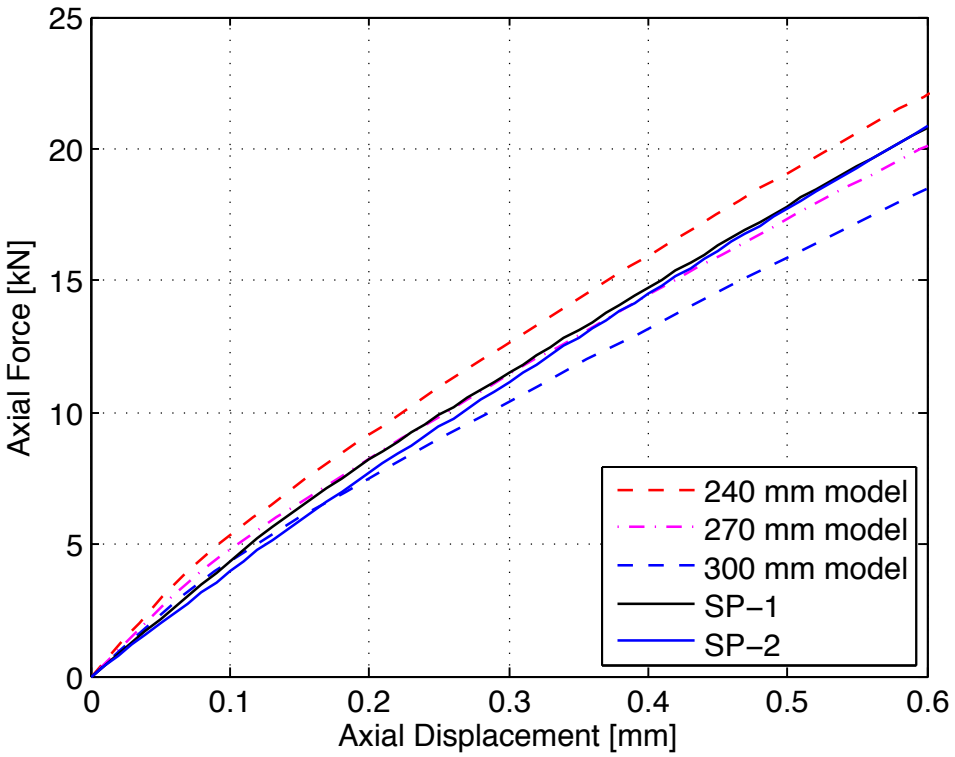

Figure 5.1.1: Force-displacement comparison with various length panels

The postbuckled range of the test data closely follows the force-displacement response of the 270 mm model. However, the slope of both curves correlates with the shorter length, 240 mm baseline model. At 0.6 mm axial displacement, the baseline

model over-estimated the reaction force by 6%, and the 270 mm model underestimates the force by 3%. Although the 270 mm model gave a more accurate result at 0.6 mm displacement, the 240 mm baseline model approximated the slope better. This suggested the 240 mm model most accurately models the actual boundary conditions within the postbuckled range.

As shown in Figures 5.1.2 to 5.1.5, the displacement field of the specimen was well predicted by the baseline model. The single half-sine wave buckled shape is the same on the skin edges and the blade section. Figures 5.1.6 to 5.1.9 show the amplitude of the out-of-plane displacements of the skin and stiffener blade under 0.6 mm axial displacement.

Figure 5.1.2: SP-1 at 0.6 mm axial displacement (front)

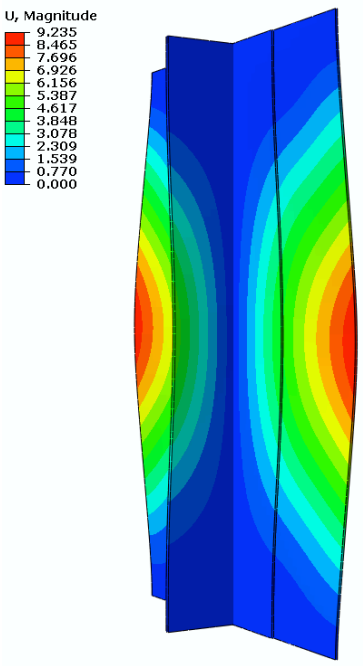

Figure 5.1.3: Baseline model out-of-plane displacement (front)

Figure 5.1.4: SP-1 at 0.6 mm axial displacement (back)

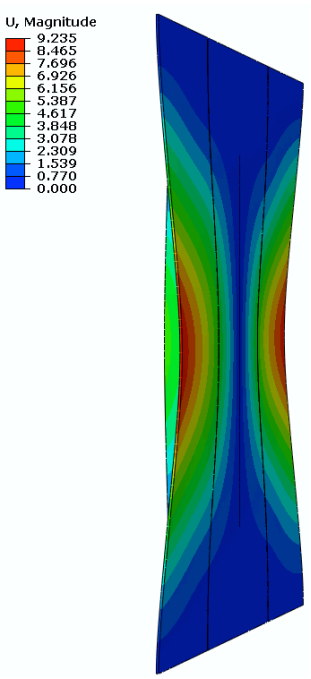

Figure 5.1.5: Baseline model out-of-plane displacement (back)

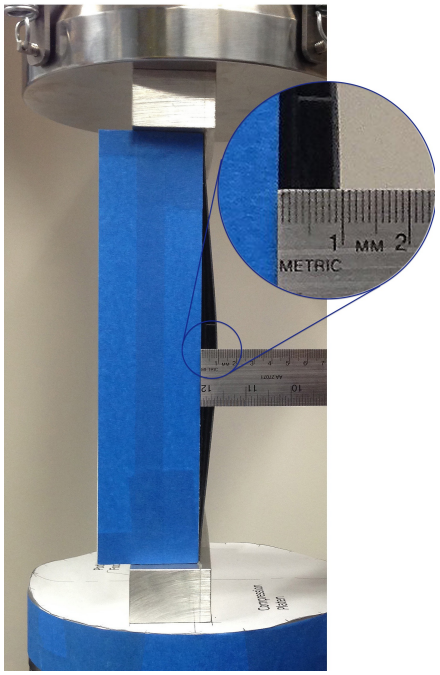

Figure 5.1.6: SP-1 out-of-plane displacement of skin at 0.6 mm

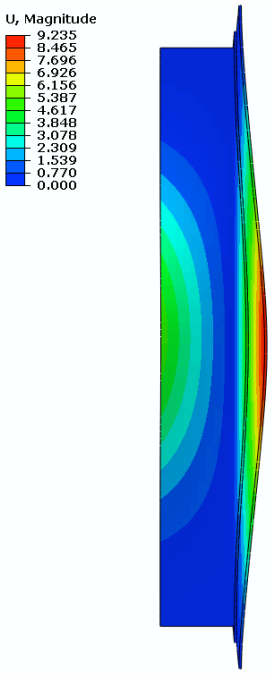

Figure 5.1.7: Baseline model skin displacement

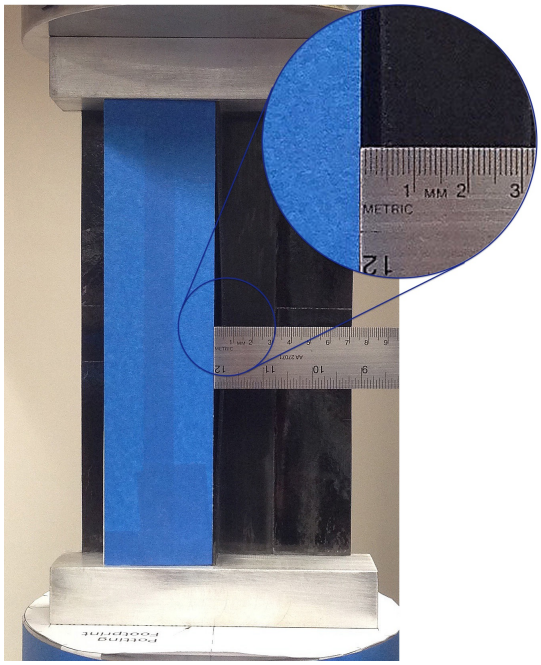

Figure 5.1.8: SP-1 out-of-plane displacement of stringer at 0.6 mm

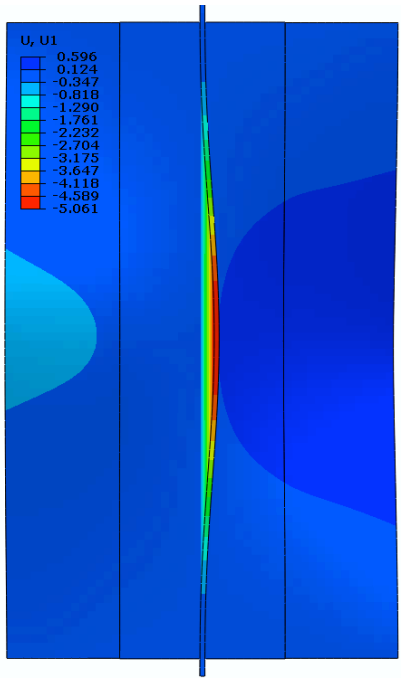

Figure 5.1.9: Baseline model stringer displacement

The progression of out-of-plane displacement of the skin plotted against the applied axial displacement is shown in Figure 5.1.10. The measurements of the SP-1 panel were taken to the nearest 0.5 mm, and showed good correlation with the test data. The onset of out-of-plane displacement of SP-1 occurs with approximately 0.05 mm additional axial displacement than the baseline model, which remains constant throughout the postbuckling range. This can be attributed to the discrepancy in modeling of the aluminum potting as a fully clamped boundary condition. At the final displacement level of 0.6 mm, the baseline finite element model over-estimated the out-of-plane displacement by 7%. Considering out-of-plane displacements vs. axial force, rather than axial displacement, yields a prediction over-estimate of only 2.5% at the final load level.

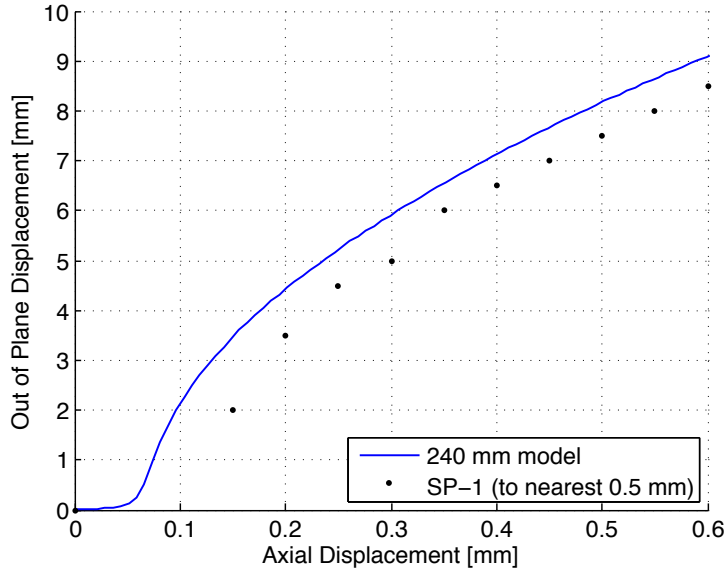

Figure 5.1.10: Skin out-of-plane displacement vs. model

The force-displacement data of the tests compared with the model including the Teflon separation, shown in Figure 5.1.11, show good agreement. At an axial displacement of 0.6 mm, model 10 shows a force 4% higher than the test data.

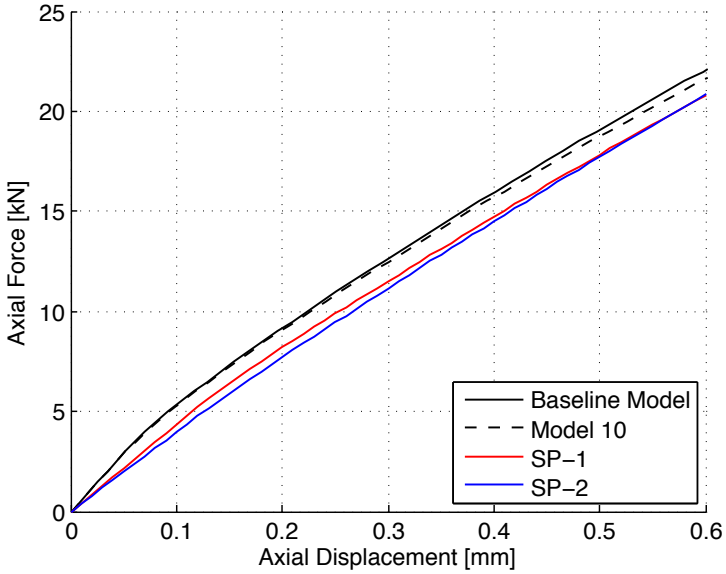

Figure 5.1.11: Model 10 comparison with test specimens

Chapter 6 - Conclusion

An investigation that involved compression testing and finite element modeling was done to determine the characteristics of the postbuckling response of the single blade-stringer specimen. The baseline eigenvalue analysis was performed to give the buckling loads and displacements, as well as mode shapes for the first 4 buckling modes of the panel. The baseline analysis then considered the highly nonlinear postbuckling response of the first mode shape of the panel by incorporating a 0.05 mm scaled imperfection of the first mode shape. The analysis determined the panel would buckle at a load of 4,047 N, and the buckle would increase in magnitude with an increase in loading. The pattern continued to the predicted onset of fiber compression type failure in the bottom ply of the skin, according to Hashin Failure Criterion, at a load of 38,628 N. If the panel was resistant to interlaminar failure, as in the baseline model, it could maintain a load 8.5 times greater than the initial buckling load. However, the tests confirmed a capacity of a minimum of 3.5 times the buckling load. Subsequent analyses studied the effect of the scale of the mode shape imperfection, different panel lengths, as well as the different mode shapes and if they experienced a mode switch in the postbuckling response.

Considering the effect of the amplitude of imperfections within the model was important because of the uncertainty in the exact configuration of the panels used in the experiments. Several models with varying imperfection magnitudes were

compared and yielded little to no effect on the postbuckling response and only a slight decrease in predicted buckling load.

Due to the complex interactions of the composite specimen and the aluminum potting, the boundary conditions were modeled as clamped, only allowing axial shortening of the specimen. Modeling different effective lengths of the panel proved to be a major contributing factor to the postbuckling response of the panel. Modeling the effective length of the panel 30 mm, and 60 mm longer, resulted in a decrease in the force-displacement response of the panel by 8%, and 14%, respectively.

The difference in imperfection mode shapes included in the models proved to be another substantial contribution to the postbuckling response of the panel. Because of the unknown initial small variations within the panel, the panel had the potential to buckle and postbuckle in several different mode configurations. The first mode remained stable to the point of first-ply failure, as well as the second mode. The third mode however experienced a mode switching to the first mode shape, where it then postbuckled according to the first mode shape. The fourth mode remained stable to the point of first-ply failure and subsequently changed to the second mode configuration. This suggests the panel strength, as well as postbuckling stiffness, is sensitive to initial imperfections.

The models, which considered the Teflon separation in the panel, showed similar results to the pristine models, although interlaminar failure was not accounted for in any of the models. The Teflon models, which consisted of a mode 1 and mode 2

response, had very similar postbuckling force-displacement relations as the respective models without Teflon, and showed only a slight decrease in stiffness. However, the presence of the Teflon separation did suggest the first-ply failure would occur at significantly lower loads than the panels without Teflon separation. Interlaminar failure, including delamination, is expected to be more important than in-ply failures, and lead to a decreased load capacity of the panel.

The repeated experimental compression tests done on two nominally identical panels, showed no degradation to a load of 21 kN and yielded similar results to those predicted by the finite element models. The force-displacement response of both panels showed the buckling load to be approximately 1.5 times the predicted buckling load. The specimens buckled according to the first predicted mode shape by the finite element models. Both specimens postbuckling force-displacement responses were also very similar to the finite element models, remaining within the prediction from the 240 mm baseline model and the 270 mm model. Under the 0.6 mm axial displacement, both test panels showed the same reaction force, while the 240 mm baseline model over-estimated the reaction force by 6%, and the 270 mm model underestimated the reaction force by 3%. The double-shell model, including the Teflon insert, overestimated the reaction force at 0.6 mm displacement by less than 4%.

The complex postbuckling behavior of a single, blade-stiffened composite panel under quasi-static compression loading can be predicted with a relatively simple, and computationally inexpensive finite element model. Aside from material properties,

and dimensions, the most important characteristics of modeling the panel are the boundary conditions, as well as the knowledge of any initial imperfections within the panel, regardless of magnitude. First-ply failure is an important aspect to determining the collapse load of the panels, but interlaminar failure should also be accounted for. Future development of this topic should include the interlaminar failure, and damage propagation, as this has been shown in previous studies to be a major contributing parameter to collapse. In addition, to investigating the single-stringer panels, relations to larger multi-stringer panels should be explored.

The panels have shown to maintain loads well into the postbuckling range, exhibiting no failure. This demonstrates the capability of stiffened panels to operate safely in the postbuckling range. Utilizing this strength reserve could significantly increase the allowable design limits for stiffened structures. This would lead to the design of thinner components, reducing overall weight and cost of aircraft.

References

[1] Daniel, I.M., Ishai, O., *Engineering Mechanics of Composite Materials*, 2nd ed., Oxford University Press, New York, 2006.

[2] Riks, E., Rankin, C.C., Brogan, F.A., "On the Solution of Mode Jumping Phenomena in Thin-Walled Shell Structures," *Computer Methods in Applied Mechanics and Engineering*, Vol. 136, No. 1-2, 1996, pp. 59-92.

[3] Falzon, B.G., Hitchings, D., "Capturing Mode-Switching in Postbuckling Composite Panels Using a Modified Explicit Procedure," *Composite Structures*, Vol. 60, No. 4, 2003, pp. 447-453.

[4] Hilburger, M.W., Starnes, J.H., "Effects of Imperfections on the Buckling Response of Compression-Loaded Composite Shells," *International Journal of Non-Linear Mechanics*, Vol. 37, No. 4-5, 2002, pp. 623-643.

[5] Wullschleger, L., Meyer-Piening, H.R., "Buckling of Geometrically Imperfect Cylindrical Shells – Definition of a Buckling Load," *International Journal of Non-Linear Mechanics*, Vol. 37, No. 4-5, 2002, pp. 645-657.

[6] Bisagni, C., "Numerical Analysis and Experimental Correlation of Composite Shell Buckling and Post-Buckling," *Composites: Part B*, Vol. 31, No. 8, 2000, pp. 655-667.

[7] Zimmermann, R., Klein, H., Kling, A., "Buckling and Postbuckling of Stringer Stiffened Fibre Composite Curved Panels," *Composite Structures*, Vol. 73, No. 2, 2006, pp. 150-161.

[8] Degenhardt, R., Kling, A., Rohwer, K., Orifici, A.C., Thomson, R.S., "Design and Analysis of Stiffened Composite Panels Including Post-Buckling and Collapse," *Computers and Structures*, Vol. 86, No. 9, 2008, pp. 919-929.

[9] Orifici, A.C., Thomson, R.S., Herszberg, I., Weller, T., Degenhardt, R., Bayandor, J., "An Analysis Methodology for Failure in Postbuckling Skin-Stiffener Interfaces," *Composite Structures*, Vol. 86, No. 1-3, 2008, pp. 186-193.

[10] Orifici, A.C., Shah, S.A., Herszberg, I., Kotler, A. Weller, T., "Failure Analysis in Postbuckled Composite T-Sections," *Composite Structures*, Vol. 86, No. 1-3, 2008, pp. 146-153.

[11] Orifici, A.C., Zarate Alberdi, I.O., Thomson, R.S., Bayandor, J., "Compression and Post-Buckling Damage Growth and Collapse Analysis of

Flat Composite Stiffened Panels," *Composites Science and Technology*, Vol. 68, No. 15-16, 2008, pp. 3150-3160.

[12] Orifici, A.C., Thomson, R.S., Degenhardt, R., Bisagni, C., Bayandor, J., "A Finite Element Methodology for Analysis Degradation and Collapse in Postbuckling Composite Aerospace Structures," *Journal of Composite Materials*, Vol. 43, No. 26, 2009, pp. 3239-3263.

[13] Bisagni, C., Vescovini, R., Dávila, C.G., "Single-Stringer Compression Specimen for the Assessment of Damage Tolerance of Postbuckled Structures," *Journal of Aircraft*, Vol. 48, No. 2, 2011, pp. 495-502.

[14] Vescovini, R., Dávila, C.G., Bisagni, C., "Failure Analysis of Composite Multi-Stringer Panels Using Simplified Models," *Composites Part B: Engineering*, Vol. 45, No. 1, 2013, pp. 939-951.

[15] Kang, J.H., Kim, C.G., "Minimum-Weight Design of Compressively Loaded Composite Plates and Stiffened Panels for Postbuckling Strength By Genetic Algorithm," *Composite Structures*, Vol. 69, No. 2, 2005, pp. 239-246.

[16] Abaqus 6.13 Users Manual, Dassault Systèmes, Providence, RI, 2013.

[17] Matlab R2013a Users Manual, The MathWorks, Natick, MA, 2013.